

# Contents

2	1	Experimental results	2
3		<i>Diamond irradiation study</i>	
4	1.1	Measurement setup . . . . .	3
5	1.1.1	Preamplifiers . . . . .	3
6	1.1.2	Diamond samples . . . . .	5
7	1.1.3	Readout devices . . . . .	6
8	1.1.4	Setup for the efficiency study using $\beta$ particles . . . . .	6
9	1.1.5	Room temperature $\alpha$ -TCT setup . . . . .	7
10	1.1.6	Cryogenic $\alpha$ -TCT setup . . . . .	7
11	1.2	Charged particle pulses and spectra . . . . .	9
12	1.2.1	Noise limitations . . . . .	9
13	1.3	Radiation limitations . . . . .	11
14	1.3.1	Quantifying radiation damage in diamonds . . . . .	11
15	1.3.2	Long-term measurement stability . . . . .	15
16	1.4	Temperature limitations . . . . .	21
17	1.4.1	Temperature-variant $\alpha$ -TCT before irradiation . . . . .	22
18	1.4.2	Temperature-variant $\alpha$ -TCT after irradiation . . . . .	23
19	1.5	Conclusion . . . . .	31

<sup>20</sup> **Chapter 1**

<sup>21</sup> **Experimental results**

<sup>22</sup> *Diamond irradiation study*

<sup>23</sup> This chapter contains the measurement results of data taken with diamond sensors.  
<sup>24</sup> First the measurement setup is described (section 1.1). Then the measured particle  
<sup>25</sup> spectra are shown in 1.2. This is followed by a study of effects of irradiation damage  
<sup>26</sup> on the electrical signal of the diamond detector and its lifetime. The last section  
<sup>27</sup> shows the results of the measurements of irradiated diamond samples at cryogenic  
<sup>28</sup> temperatures. The aim of these studies is to find the operational limitations of dia-  
<sup>29</sup> mond detectors for spectroscopy and tracking applications. The studies compare the  
<sup>30</sup> experimentally acquired data with the theory from the previous chapter and define  
<sup>31</sup> limitations of the diamond detectors in terms of noise, radiation and temperature.

<sup>32</sup> Diamond sensors are mainly used for two types of measurements: particle counting  
<sup>33</sup> and spectroscopy. The first type of measurements depends on the sensor's efficiency –  
<sup>34</sup> the ability to detect all or at least a known percentage of radiation quanta (particles  
<sup>35</sup> or photons) that hit it. The energy of the radiation is not so important; what bears  
<sup>36</sup> the information is the rate and the spatial distribution. Here the radiation does  
<sup>37</sup> not necessarily stop in the bulk, but rather continues its way. In spectroscopy, on  
<sup>38</sup> the other hand, the idea is that a particle stops within the sensor, depositing all  
<sup>39</sup> its energy, which is then measured via the freed charge carriers. The aim of the  
<sup>40</sup> experiments described in this chapter is to:

- <sup>41</sup> 1. Quantify the efficiency of the sCVD diamond in counting mode,
- <sup>42</sup> 2. Quantify the degradation of efficiency with respect to the received radiation  
<sup>43</sup> dose,
- <sup>44</sup> 3. Quantify the macroscopic effects on charge carrier behaviour with respect to  
<sup>45</sup> the received radiation dose and
- <sup>46</sup> 4. Define limitations for its use in spectroscopy.

<sup>47</sup> The results discussed here show that there are several limitations for using diamond as  
<sup>48</sup> a measurement device. All of them need to be taken into account for the measurement

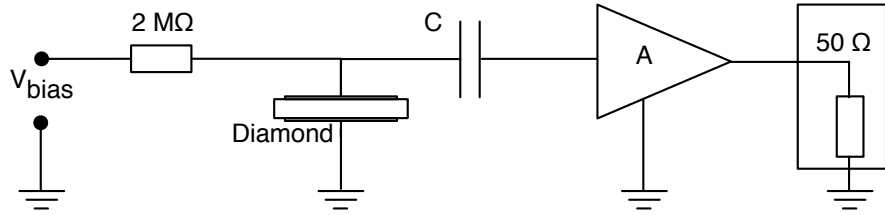


Figure 1.1: Diagram of a diamond detector readout chain.

device to perform reliably and stably. The first step is to build a setup that is insensitive to external electromagnetic interferences and minimises electrical noise in the system. The setup needs to be calibrated before use. Then, the measurement conditions have to be defined, such as the temperature, the type of radiation and its flux. This allows us to estimate the lifetime of the detector and predict the longterm change of the signal. This change can then be accounted for when interpreting the output data.

## 1.1 Measurement setup

To get reliable measurement results, great care has to go towards designing a measurement setup that minimises the noise in the measurements. Shielding has to be applied wherever possible. For instance, aluminium foil can be wrapped around the exposed parts of the system to shield them from external radio-frequency (RF) interferences. In addition, the sensors have to be covered to prevent the light from shining directly onto them. The incident photons can deposit enough energy to increase the leakage current of the detector.

The measurements using diamond that are explained in these chapters were carried out using several measurement setups, but they are all similar in terms of the electrical signal chain. The measurement chain consists of three main parts: a diamond sensor, a signal preamplifier and a readout device, as seen in diagram 1.1. The signals propagating along the analogue chain (before being digitised by the readout device) are fast – in the GHz bandwidth range – and with low amplitudes – of the order of tens of  $\mu\text{V}$ . This gives rise to importance of RF shielding. Also, the connection between the carrier and the preamplifier has to be as short as possible to avoid capacitive signal losses in the transmission line. Finally, the system needs to be grounded properly.

### 1.1.1 Preamplifiers

Two preamplifiers are used for the measurements, one sensitive to charge and the other to current. *CIVIDEC Cx* (figure 1.2a) is a charge sensing amplifier. Its high SNR (equivalent noise charge of  $300 + 30 \text{ pF}^{-1} \text{ e}^-$  and a reported gain of  $\sim 12 \text{ mV/fC}$ ) makes it a good choice for spectroscopic measurements with diamond

## 1.1. MEASUREMENT SETUP

---

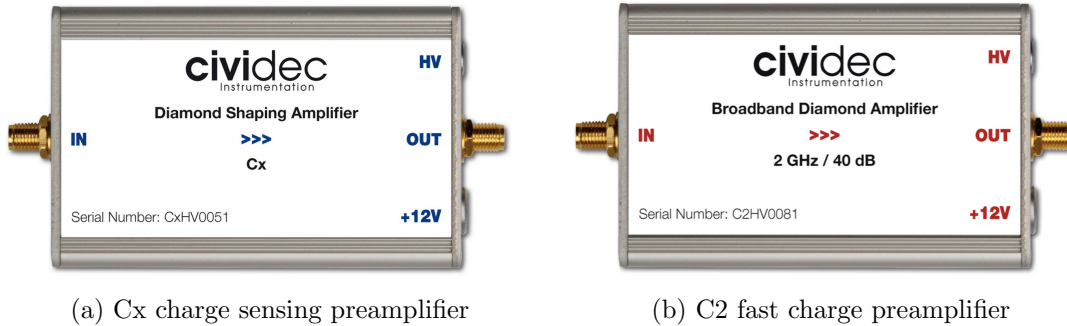


Figure 1.2: Amplifiers used for the charge and current measurements

78 sensors. *CIVIDEC C2* (figure 1.2b) is a fast current preamplifier with a 2 GHz band-  
 79 width limit. It is used for TCT measurements because of its fast response and a good  
 80 SNR. Both are embedded in an RF-tight aluminium box to reduce the noise pickup.  
 81 Both have an AC coupled input and an output with a  $50 \Omega$  termination.

### 82 Calibration

83 The amplifiers have to be calibrated before use to determine their gain. Both are  
 84 calibrated using a square signal generator with a known amplitude step of  $U_{\text{in}} =$   
 85  $(252 \pm 5)$  mV. A 2 GHz oscilloscope with a 10 GS/s sampling is used to carry out  
 86 these measurements.

87 In the case of the Cx charge sensitive amplifier, the signal is routed through a  
 88 capacitor with a calibration capacitance  $C_{\text{cal}} = (0.717 \pm 0.014)$  pF and then to the  
 89 input of the amplifier. The pulse area behind the capacitor is  $a_{\text{cal}} = (5.0 \pm 0.5)$  pVs,  
 90 with the signal amplitude on the output amounting to  $U_{\text{Cx}} = (1.95 \pm 0.05)$  V. The  
 91 input voltage step combined with the calibration capacitance yields a calibration  
 92 charge  $Q_{\text{cal}} = C_{\text{cal}} \cdot U_{\text{in}} = (181 \pm 5)$  fC. The gain of the Cx amplifier is therefore  
 93  $A_{\text{Cx}}^Q = \frac{U_{\text{Cx}}}{Q_{\text{cal}}} = (9.3 \pm 0.4)$  mV/fC or  $A_{\text{Cx}}^a = \frac{U_{\text{Cx}}}{a_{\text{cal}}} = (390 \pm 40)$  mV/pVs. The area-based  
 94 amplification factor has a higher uncertainty ( $\sim 10\%$ ) than the amplitude-based  
 95 factor ( $\sim 4\%$ ) due to the measurement limitations of the oscilloscope. Nevertheless,  
 96 it can be used as an estimate for the integrated charge of a current pulse.

97 To calibrate the C2 current amplifier, only the amplitude gain has to be measured.  
 98 The input signal amplitude has to be such that it keeps the output amplitude within  
 99 the amplifier's linear range, that is  $\pm 1$  V. The signal from the generator is therefore  
 100 routed through a 36 dB attenuator to decrease its amplitude to  $U_{\text{inAtt}} = (3.95 \pm$   
 101  $0.05)$  mV. Two amplifiers with different gains have been measured, because both  
 102 are used for the measurements at different times. The output of the first amplifier  
 103 amounts to  $U_{\text{C2-1}} = (860 \pm 5)$  mV. This yields the amplification gain equal to  $A_{\text{C2-1}} =$   
 104  $\frac{U_{\text{inAtt}}}{U_{\text{C2-1}}} = (217 \pm 3)$ . The second amplifier has the output equal to  $U_{\text{C2-2}} = (632 \pm 5)$  mV  
 105 with the gain equal to  $A_{\text{C2-2}} = (152 \pm 3)$ .

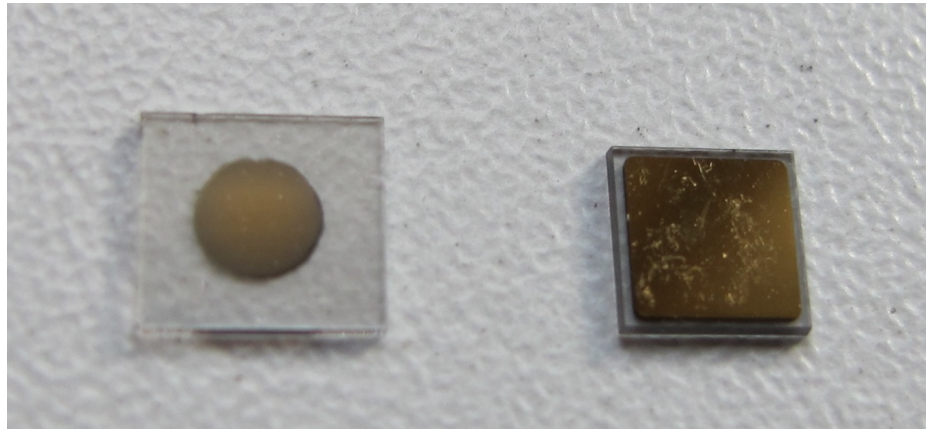


Figure 1.3: Two scCVD diamond samples: A IIa 1scdhq (left) and an E6 S37 (right)

### <sup>106</sup> 1.1.2 Diamond samples

<sup>107</sup> Detector-grade diamonds are very difficult to produce, mostly because it is very diffi-  
<sup>108</sup> cult to ensure a high enough purity of the lattice. The sensor samples used for these  
<sup>109</sup> studies were bought at Element Six (E6) [2]. They all have the same standard dimen-  
<sup>110</sup> sions. sCVD diamonds with dimensions  $4.7 \times 4.7 \text{ mm}^2$  are already sufficiently large  
<sup>111</sup> for most of the beam monitoring applications and still affordable. One of the samples  
<sup>112</sup> with dimensions of  $5.6 \times 5.3 \text{ mm}^2$  produced by IIa Singapore [3] was also sent to CERN  
<sup>113</sup> to be characterised. The target thickness for all the samples is  $500 \mu\text{m}$ . Diamonds  
<sup>114</sup> this thick yield a high enough signal-to-noise ratio for MIPs to be measured by the  
<sup>115</sup> electronics. Table 1.1 shows all the samples used for this study. Two of them were  
<sup>116</sup> later irradiated with 300 MeV pions and then compared to the pre-irradiated state.  
<sup>117</sup> Irradiation doses for damaging the material need to be high – above  $10^{12}$  particles  
<sup>118</sup> per  $\text{cm}^2$  to be able to observe change in the sensor’s behaviour.

<sup>119</sup>	Name	Type	Producer	Dimensions [ $\text{mm}^2$ ]	Thickness [ $\mu\text{m}$ ]	Electrode	Irradiated
	S37	sCVD	E6	$4.7 \times 4.7$	548	Cr/Au	no
	S50	sCVD	E6	$4.7 \times 4.7$	537	Cr/Au	no
<sup>120</sup>	S52	sCVD	E6	$4.7 \times 4.7$	515	Cr/Au	$1 \times 10^{14} \pi \text{ cm}^{-2}$
	S79	sCVD	E6	$4.7 \times 4.7$	529	Cr/Au	$3.63 \times 10^{14} \pi \text{ cm}^{-2}$
	ELSC	sCVD	E6	$4.7 \times 4.7$	491	Cr/Au	no
	1scdhq	sCVD	IIa	$5.6 \times 5.3$	460	Cr/Au	no

<sup>121</sup> Table 1.1: Diamond sensor samples used

<sup>122</sup> The diamond samples have quoted impurity densities of  $\leq 2 \times 10^{14} \text{ cm}^{-3}$  and nitro-  
<sup>123</sup> gen incorporation of  $\leq 1 \text{ ppb}$ . The electrodes were added by various companies and  
<sup>124</sup> institutes. For instance, S52 was metallised by a company DDL (now defunct) while  
<sup>125</sup> the Physics Department of the University of Firenze, Italy metallised the S79. There  
<sup>126</sup> are also several techniques for producing the electrodes. The DDL contacts consist  
<sup>127</sup> of three layers: DLC (diamond-like carbon)/Pt/Au with 4/10/200 nm thicknesses,  
<sup>128</sup> respectively. The metallisation for S79, on the other hand is made up of Cr/Au with

## 1.1. MEASUREMENT SETUP

---

a total thickness of  $\sim$ 400 nm. The area coverage also differs from sample to sample. Diamonds must not be metallised until the very edge as the proximity of contacts with a high potential can lead to sparking. However, the areas not covered by the metallisation are less efficient because the fringe fields at the edges are not as strong as in the middle. This effectively reduces the sensitive area of the sensors. In the diamonds used here the effective area was anywhere from  $9\text{ mm}^2$  to  $18\text{ mm}^2$ . Leakage current through the bulk was below 1 ns, but increased for the irradiated samples. The capacitance was of the order of  $(2.0 \pm 0.3)\text{ pF}$ .

### 1.1.3 Readout devices

Electrical signals in diamond detectors are in the GHz frequency range. To preserve this information, the readout device has to have a high bandwidth limit. For instance, a 250 MHz limit is enough for the spectroscopic measurements with the Cx charge amplifier, but might be insufficient for the current measurements with the C2 amplifier. Two devices are used take data shown in this chapter. The first choice is a 2 GHz LeCroy WaveRunner 204MXi-A. This specific model has a high enough limit for the fast current preamplifier signals. It offers a versatile solution for analogue signal readout – it is fast to set up and reliable. It is very convenient for use in lab tests and for experiments where small amounts of data are taken and where speed is not crucial. However, its slow acquisition speed turns out to be a bottleneck in the test beam experiment. Its initial 100 Hz readout rate decreases to a mere 20 Hz within 20 minutes, because every single trigger is saved as a separate file and the Windows operating system is not capable of handling 10000+ files in a single directory easily. This is why it has been exchanged with a DRS4 [1], an analogue readout device developed by PSI, Switzerland. This compact device is capable of recording up to four waveforms at a time at a steady rate of up to 500 Hz. Its 700 MHz bandwidth limitation is sufficient for the signal from the charge amplifier.

### 1.1.4 Setup for the efficiency study using $\beta$ particles

The efficiency study of the diamond sensors has been carried out at CERN in the North Hall test beam facility. There a straight high-energy particle beam of  $\pi_{120}\text{ GeV}$  is provided to the users to calibrate their detectors. The beam had a transverse spread of  $\sigma = 10\text{ mm}$  in both axes. The particle rate is of the order of  $10^4\text{ }\pi\text{ cm}^{-2}\text{ s}^{-1}$ . A diamond sensor embedded in a PCB carrier has been placed in the beam spot perpendicular to the beam and connected via an SMA connector directly to a charge amplifier (described below). The amplified signal is read out using a LeCroy oscilloscope and a DRS4 analogue readout system (both described below). A computer is used as a controller and data storage for the readout device. A beam telescope is used as a reference detector. It is a device that helps to cross-check the measurements of the devices under test (DUTs) and to carry out spatially resolved studies on the DUTs. It consists of several pixellated sensor planes placed in series, which can track a particle's trajectory with a precision of a few  $\mu\text{m}$ . The sensor planes are positioned

in front of the DUT and behind it. Then the beam telescope acts as a trigger system – it triggers the readout of both the telescope data and DUT data when both the planes in front and behind the DUT recorded a hit by the impinging particle. A particle detected by all the planes within the DUT window and the DUT itself counts towards its efficiency whereas a hit missed by the DUT means that the DUT is not 100 % efficient. To discard the hits that miss the DUT completely, a region of interest (ROI) can be chosen in the beam telescope planes. The equation for calculating the sensor efficiency is therefore

$$\epsilon = \frac{N_{\text{DUT}} \wedge N_{\text{telescope}}}{N_{\text{telescope}}} \quad (1.1)$$

for an ROI smaller than the sensitive region of the diamond.

### 1.1.5 Room temperature $\alpha$ -TCT setup

This TCT study is a follow-up of an extensive diamond TCT study at cryogenic temperatures [13]. The room-temperature TCT measurements have been carried out in the lab. The setup consists of a diamond sensor embedded in a PCB carrier, a current amplifier and an oscilloscope. To measure  $\alpha$  particles, their energy loss during their trajectory has to be minimised. Therefore the diamond is placed inside a vacuum chamber. The chamber is a steel tube with a diameter of 5 cm. On one side it is connected to a vacuum pump via a steel pipe. A feedthrough with an SMA connector is placed on the other side. A C2 current amplifier is connected directly onto the feedthrough. The amplified output is connected to the oscilloscope via an SMA cable. An  $^{241}\text{Am}$  source with a diameter of 2 cm and a height of 0.5 cm is fixed onto the sensor carrier (figure 1.4a, figure 1.4b). Then the carrier is inserted in the chamber and fixed in place using an air-tight clamp. The pump can then be switched on. It is capable of providing the inside pressure as low as  $10^{-4}$  mbar after approximately one hour of operation, but measurements can take place even after five minutes of evacuation, at around  $10^{-3}$  mbar. The most important thing to bear in mind is to switch the bias voltage of the sensor OFF during the process of evacuation, because the gas becomes more conductive at the pressure of the order of  $10^{-1}$  mbar, which is at the bottom of Paschen's curve [9]. A failure to switch off the bias voltage may cause a spark between the signal and ground line, destroying the amplifier.

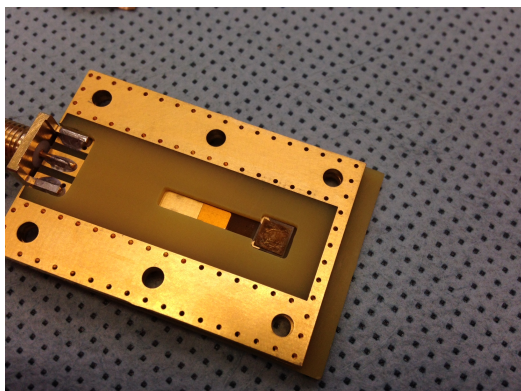
### 1.1.6 Cryogenic $\alpha$ -TCT setup

The experiment at cryogenic temperatures has been carried out in the cryolab at CERN. The room-temperature TCT setup has to be modified to allow for measurements at temperatures as low as 2 K. It consists of three parts:

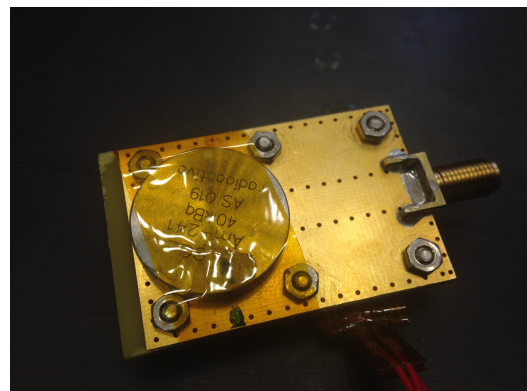
- 202 1. a cryostat – a thermally insulated cylinder capable of containing liquid helium,
- 203 2. an inlet – an air-tight mechanical tube with valves and feedthroughs at the top  
204 that is lowered in the liquid helium and

## 1.1. MEASUREMENT SETUP

---



(a) PCB carrier with an embedded diamond sample



(b) Radioactive source over the carrier

Figure 1.4: Positioning of the  $\alpha$ -source on top of the sensor carrier

- 205     3. the diamond sample embedded in a PCB carrier with a fitted temperature  
206     sensor, a heater and cables leading to the feedthroughs.

207     The setup is described in detail in [13].

208     When the diamond sample is placed in the PCB carrier and the  $^{241}\text{Am}$  source is in  
209     place, the inlet is sealed and lowered in the empty cryostat. Then the inside volume  
210     of the inlet is evacuated to down to  $10^{-5}$  mbar while the liquid helium is flowing into  
211     the cryostat. To improve the thermal contact between the diamond and the coolant,  
212     a small amount of helium gas is added inside the evacuated inlet, setting the vacuum  
213     to around  $10^{-3}$  mbar. This value changes with time, because the gas condenses on  
214     the walls of the inlet, reducing the number of floating particles. For this reason the  
215     helium gas has to be added on an irregular basis. Every addition causes a significant  
216     undershoot of the sample temperature, which had to be corrected for using a heater  
217     placed on the back of the PCB carrier. Also, the added gas deteriorates the vacuum  
218     inside the inlet. It is very important to monitor the pressure so as not to let it rise  
219     above  $10^{-2}$  mbar. The gas at this pressure is significantly more conductive and could  
220     cause a short circuit between the two diamond plates or in the SMA connectors,  
221     destroying the amplifier. Furthermore, at approximately 60 K the helium gas has to  
222     be evacuated from the inlet to avoid a potential explosion due to the expansion of  
223     the gas with temperature.

224     When the sample is cooled to the minimum temperature achievable by means  
225     of liquid helium without over-pressurising it (4.2 K), the measurements start. A  
226     temperature sensor placed on the back of the PCB carrier is used to measure the  
227     temperature of the sample. After every temperature data point, the current through  
228     the heater placed in the PCB next to the diamond sample is increased, warming up  
229     the sample. The initial temperature time constant of the order of tenths of seconds at  
230     low temperatures increases with temperature. Even more so when helium is evacuated  
231     from the inlet at 60 K, removing the thermal bridge between the wall of the inlet and  
232     the diamond sample. At the room temperature (RT), the time constant increases to

233 the order of minutes.

## 234 1.2 Charged particle pulses and spectra

235 In previous chapter the ionisation profiles for different types of radiation were dis-  
236 cussed. It is known that  $\beta$  and  $\gamma$  radiation induces a triangular electric pulse whereas  
237  $\alpha$  radiation induces a rectangular one. However, their amplitude, width and rise/fall  
238 time depend heavily on the type of interaction with the diamond, the purity of the  
239 diamond and the bandwidth of the amplifier and the oscilloscope. This section shows  
240 the signal pulses of  $\alpha$ ,  $\beta$  and  $\gamma$  radiation with their respective energy distributions for  
241 the case of a diamond detector. Then follows a discussion of effects of noise on these  
242 measurements.

243 A CIVIDEC C2 current amplifier together with the LeCroy oscilloscope (both  
244 with a bandwidth limit of 2 GHz) has been used to record the pulse shapes whereas  
245 the Cx charge amplifier is used for charge measurement. A 2 GHz bandwidth limit  
246 defines the minimum rising time equal to  $t_r \simeq \frac{0.34}{BW} = \frac{0.34}{2 \times 10^9} = 170$  ps, therefore  
247 the system is capable of measuring pulses with a minimum FWHM  $\simeq 170$  ps. This  
248 already makes it impossible to measure the initial peak in the  $\alpha$  response due to the  
249 two flavours of charge carriers travelling. If a charge carrier travelling through the  
250 bulk takes  $t_{t1} \sim 6$  ns to get to the electrode on the other side ( $d_1 \sim 500$   $\mu m$ ), the  
251 carrier with the opposite charge and a shorter path to the closer electrode – max.  
252  $d_2 \sim 10$   $\mu m$  – only takes  $t_{t2} \sim \frac{d_2}{d_1} t_{t1} = 120$  ps. A drift time this short induces a  
253 current pulse that is too narrow for the C2 amplifier or the oscilloscope to be able to  
254 observe.

255 Figure 1.5 shows a set of pulses and an averaged pulse for  $\alpha$ ,  $\beta$  and  $\gamma$  radiation  
256 using an  $^{241}Am$ ,  $^{90}Sr$  and  $^{60}Co$  source, respectively. The particles are measured with  
257 the non-irradiated sCVD diamond S37.  $\alpha$  particles always produce the same signal  
258 pulse, but with a high noise RMS. The averaging suppresses the noise while still  
259 retaining most the information. It does, however, smear the rising and falling edge,  
260 increasing the rise time. The  $t_r$  is now of the order of 0.5 ns. Both  $\beta$  and  $\gamma$  pulses  
261 look similar - triangular and with a wide range of amplitudes. Here the pulse count  
262 is low, so the pulses with a high amplitude are not recorded. A trigger set very high  
263 would be needed to “catch” them with the oscilloscope.

### 264 1.2.1 Noise limitations

265 Noise is a major limiting factor in particle detection. It defines the minimum measur-  
266 able particle energy and the minimum measurement resolution. It is hence important  
267 to minimise the electric noise in the detector signal. The major noise contribution  
268 comes from poor shielding from external electromagnetic sources. These often cause  
269 ringing, whereby the signal oscillates with a frequency defined by the external source.  
270 The ringing makes high-frequency measurements impossible. Another source of noise  
271 is the sensor itself. In the case of silicon, natural light increases the number of ther-

## 1.2. CHARGED PARTICLE PULSES AND SPECTRA

---

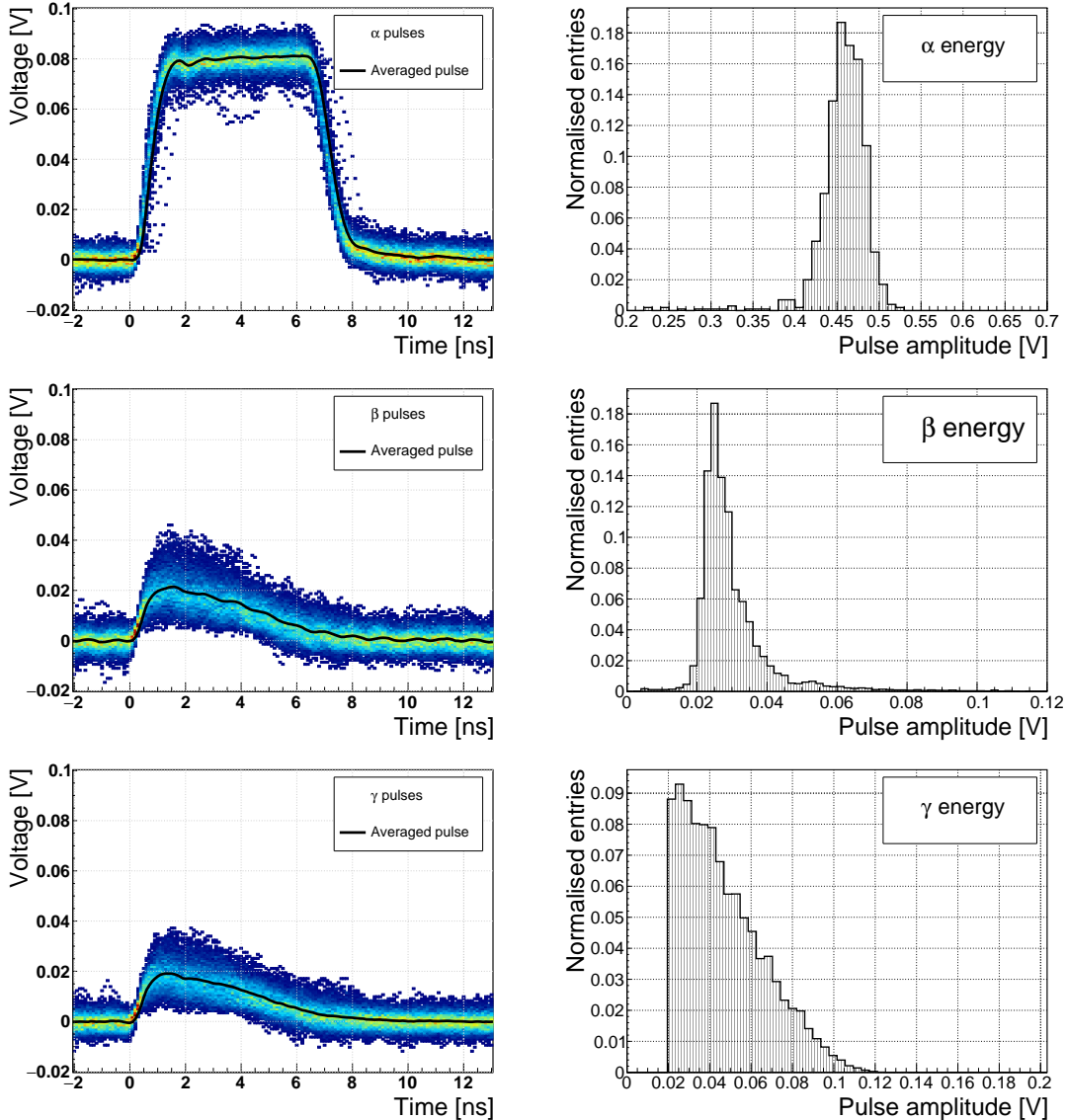


Figure 1.5: Superimposed and averaged pulses (a, b and c, current amplifier) and distributions of deposited energy (d, e, f, charge amplifier) for three types of radiation. Note the scale on the X axis of the distributions.

272 mally excited free charge carriers, increasing the leakage current. This is not the  
 273 case for diamond, which is with its high energy band gap insensitive to visible light.  
 274 Nevertheless, any noise produced by the sensors is amplified by the signal amplifiers,  
 275 which add an additional noise of the analogue electrical circuit to the amplified  
 276 signal. Finally, the digitisers add the quantisation noise to the digitised signal. If  
 277 the measurement range is significantly higher than the actual measured signal, the  
 278 quantisation noise can be a significant contributor to the decrease of the overall mea-  
 279 surement resolution.

280 **1.3 Radiation limitations**

281 Exposure to ionising radiation degrades sensors. It introduces charge traps by damag-  
282 ing the sensor material. The electrons and holes created by the impinging particle get  
283 trapped in these traps, decreasing the induced current on the electrodes. This yields  
284 a lower integrated charge in an irradiated sensor than that in a non-irradiated one.  
285 Charge collection efficiency is therefore correlated with the level of irradiation. This  
286 section contains a study of the effects of pion ( $\pi_{300}$  MeV) irradiation on the charge col-  
287 lection efficiency of sCVD diamond detectors. To carry out this study, two diamond  
288 samples were irradiated to doses of  $1 \times 10^{14} \pi \text{ cm}^{-2}$  (S79) and to  $3.63 \times 10^{14} \pi \text{ cm}^{-2}$   
289 (S52). Then a test beam campaign was carried out to observe the charge collection ef-  
290 ficiency at different bias voltage settings. The highest achieved efficiency values were  
291 used to determine the effective drop in efficiency with respect to received radiation  
292 dose. A procedure defined by a collaboration researching diamond behaviour RD42  
293 was applied to the measured values to extract the damage factor. The next subsec-  
294 tion contains measurements and results of a long-term stability study using  $\alpha$  and  
295  $\beta$  particles. In particular, the charge collection efficiency as a function of time was  
296 measured during the measurements with  $\beta$  and  $\alpha$  radiation. To investigate this effect  
297 on the scale of charge carriers, the change of TCT pulses with time was observed.  
298 Finally, a procedure that improves the pulse shape and with it the charge collection  
299 is proposed.

300 **1.3.1 Quantifying radiation damage in diamonds**

301 Radiation damage varies with the type of radiation (particles or photons) and its  
302 energy. There are several models existing [12, 11] that try to explain the impact  
303 of irradiation and to provide *hardness factors* to compare the radiation damage be-  
304 tween different particles. The standard way is to convert the damage into *neutron*  
305 *equivalent* [6]. Some models have been extensively verified with simulations and with  
306 experiments. In these experiments charge collection in sensors is measured before  
307 and after irradiation. This procedure is repeated several times, with a measurement  
308 point taken after every irradiation. When a set of measurements of charge collection  
309 is plotted against the radiation dose received by a specific particle at a specific energy,  
310 a damage factor  $k_\lambda$  can be extracted. Damage factors have to be measured across a  
311 range of energies and types of radiation to properly quantify the damage in the sen-  
312 sors. They are then compared against the simulations to verify that the experimental  
313 observations are in line with the theory.

314 Diamond is an expensive material and the technology is relatively new as com-  
315 pared to silicon. Therefore not many institutes are carrying out diamond irradiation  
316 studies. To join the efforts, the RD42 collaboration [5] was formed. It gathers the  
317 experimental data from diamond irradiation studies. Unlike with silicon, the exper-  
318 imental results so far show no significant correlation with the NIEL (non-ionising  
319 energy loss) model [12], which correlates detector efficiency with the number of lat-  
320 tice displacements. Therefore an alternative model was proposed [11], correlating

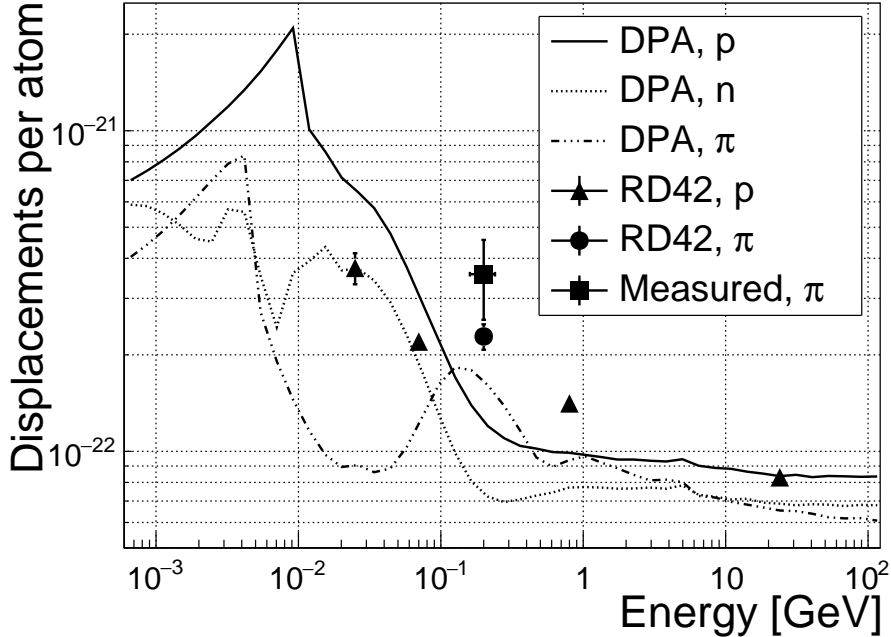


Figure 1.6: Diamond radiation damage - a model based on displacements per atom [11]. Added are data points for protons and pions by RD42 [16] and one data point for pions measured in the scope of this thesis.

the diamond efficiency with *displacements per atom* (DPA) in the bulk. Figure 1.6 shows the DPA model for a range of energies of proton, pion and neutron irradiation in diamond. According to the figure, a 300 MeV pion beam damages the diamond bulk twice as much as a 24 GeV proton beam. The data points obtained by RD42 are also added to the figure. They have been normalised to damage by 24 GeV protons. Finally, the data point measured in the scope of this thesis has been added for comparison. The calculation is done below.

### Irradiation with a $\pi_{300 \text{ MeV}}$ beam

The samples were irradiated at the Paul Scherrer Institute (PSI) [4] by means of a beam of pions with an energy of 300 MeV (kinetic energy 191.31 MeV) and with a flux of up to  $1.5 \times 10^{14} \pi \text{ cm}^{-2}$  per day. The system has a 10 % uncertainty on the beam energy. In addition, the equivalent fluence calculation has an error of  $\pm 20 \%$ . Looking at the pion damage curve in figure 1.6,  $\pi_{300 \text{ MeV}}$  point sits on a steep section of the DPA curve. This means that a deviation in beam energy can have a significant effect on the damage.

Two diamond samples, S52 and S79, were put in the  $\pi_{300 \text{ MeV}}$  beam in the 2014 PSI irradiation campaign; S52 to  $(1 \pm 0.21) \times 10^{14} \pi \text{ cm}^{-2}$  and S79 to  $(3.63 \pm 0.77) \times 10^{14} \pi \text{ cm}^{-2}$ . During the process, the golden electrodes got slightly activated, but the activation decayed in two weeks.

**340 Charge collection efficiency and charge collection distance**

**341** Three diamonds – non-irradiated S37 and irradiated S52 and S79 – were tested in  
**342** a  $\pi_{120 \text{ GeV}}$  test beam in the SPS North Experimental Area at CERN [8] before and  
**343** after irradiation. The goal was to estimate the charge collection efficiency (CCE) and  
**344** charge collection distance (CCD) as a function of irradiation dose. The samples were  
**345** primed (pumped) prior to data taking using a  $^{90}\text{Sr}$  radioactive source. The data were  
**346** then taken at a range of bias voltages ranging from 30 V to 900 V, yielding between  
**347** 0.06 V/ $\mu\text{m}$  and 1.8 V/ $\mu\text{m}$  electrical field in the bulk. Every data point contained  
**348** approximately  $5 \times 10^4$  measured particles. The charge deposited by the particles  
**349** was measured using a CIVIDEC Cx charge preamplifier. As expected, the integrated  
**350** amplitude spectrum followed a landau distribution. Its most probable value (MPV)  
**351** was used to calculate the most probable collected charge  $Q_i$ :

$$Q_i [e^-] = \frac{Q_i [fC]}{1.6 \times 10^{-4}} = \frac{MPV [mV]}{A [mV/fC]} \cdot 6.241 \times 10^4 \quad (1.2)$$

**352** where  $A = 9.2 \text{ mV/fC}$  is the preamplifier gain factor. The CCD was then calculated  
**353** using the average number of electron-hole pairs produced per micrometer in diamond  
**354**  $\delta_d = 36 \text{ e-h } \mu\text{m}^{-1}$  (from table ??):

$$CCD = \frac{Q_i}{\delta d} \quad (1.3)$$

**355** The resulting CCD for the three measured samples at bias voltages ranging from  
**356** 0.2–1.6 V  $\mu\text{m}^{-1}$  is shown in figure 1.7a. S37 exhibits full collection distance already  
**357** at 0.4 V  $\mu\text{m}^{-1}$  whereas the irradiated samples have a more gentle increase of CCD  
**358** with increasing bias voltage. It is evident that at 1 V  $\mu\text{m}^{-1}$  the maximum CCD has  
**359** not been reached in the case of S79 and S52.

**360 Irradiation damage factor**

**361** The irradiation damage factor  $k$  is a way to quantify irradiation damage of a specific  
**362** particle at a specific energy. Via this factor different types of irradiation can be  
**363** compared. It is obtained experimentally by measuring the CCD of a number of  
**364** samples at various irradiation steps and fitting the equation 1.5 to the data.  $\lambda$  is the  
**365** measured CCD,  $\lambda_0$  is the CCD of a non-irradiated sample and  $\Phi$  the radiation dose.

$$\frac{1}{\lambda} = \frac{1}{\lambda_0} + k_\lambda \cdot \Phi \quad (1.4)$$

$$\lambda = \frac{\lambda_0}{k_\lambda \lambda_0 \Phi + 1} \quad (1.5)$$

**367** The data points with the maximum CCD obtained in the test beam measurements  
**368** are plotted against radiation dose received (see figure 1.7b). Equation 1.5 is fitted  
**369** to the data points and a damage factor  $k_\lambda = (3.0 \pm 1.0) \times 10^{-18} \text{ } \mu\text{m}^{-1} \text{ cm}^{-2}$  was  
**370** obtained. This value is for a factor of two higher than the damage factor obtained

### 1.3. RADIATION LIMITATIONS

---

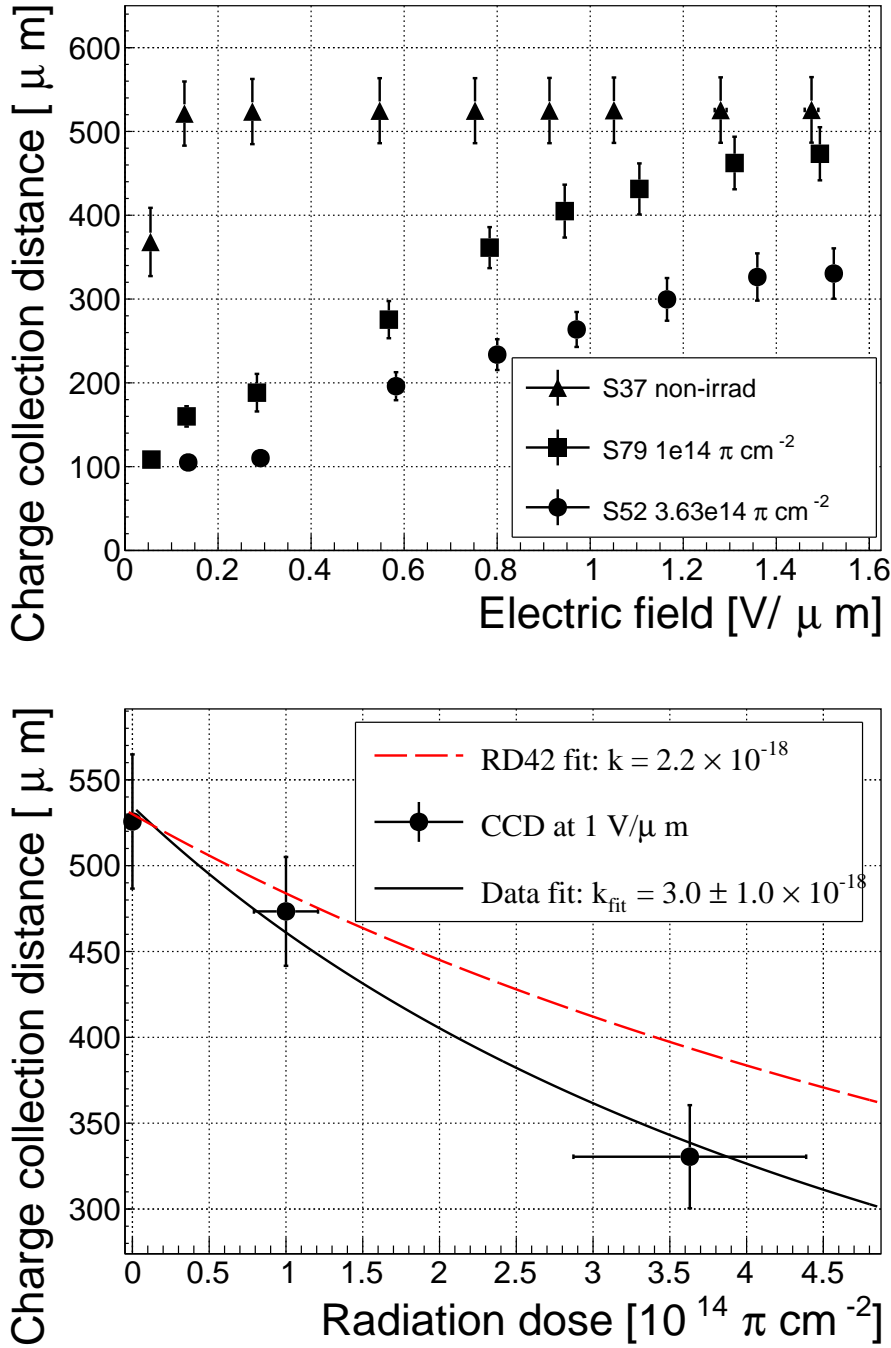


Figure 1.7: First figure shows the CCD for S37, S79 and S52 at a range of bias voltage settings. The charge collection distance at 500 V bias voltage for the three diamond samples is then compared to the RD42 data for pion irradiation in the second figure. The data points are about 5–15 % lower than expected from the RD42 data [16].

<sup>371</sup> by RD42. Also, with only two samples measured, the statistical uncertainty is high.  
<sup>372</sup> Nevertheless, it can be concluded that the 300 MeV pions damage the diamond bulk

373 more than the 24 GeV protons.

### 374 **1.3.2 Long-term measurement stability**

375 An important requirement for particle detectors is a stable performance over long  
376 periods of time. For instance, the charge collection for a defined radiation type and  
377 quantity must not change over time or has to change in a predicted way. Diamonds  
378 are stable as long as their environment and their operating point does not change  
379 significantly. The stability of diamond detectors depends on many factors (material  
380 purity, polishing process, electrode material, irradiation damage etc.). The aim is  
381 to study the behaviour of diamond under controlled conditions, with the goal to  
382 understand its limitations. One of these limitations is for sure the received radiation  
383 dose as it can affect the long-term stability of the sensor during operation.

384 The three diamond samples (S37, S79 and S52) have been exposed to two different  
385 types of ionising radiation for a longer period to see if their behaviour changes over  
386 time. Two parameters have been observed in particular:

- 387 1. Charge collection of  $\beta$  particles and
- 388 2. Charge collection and ionisation profile of  $\alpha$  particles.

389 The results in this and in the next section will show that, in both cases, priming plays  
390 an important role in improving the diamond measurement stability.

#### 391 **$\beta$ long-term stability**

392 The diamond samples have undergone a long-term stability test using  $\beta$  radiation.  
393 This has been done using a  $^{90}\text{Sr}$  source emitting  $\sim 2$  MeV electrons at a rate of  
394 approximately  $10^4 \text{ e}^- \text{ cm}^{-2}$ . To simulate the initial conditions in HEP experiments,  
395 the sensors must not be primed before starting the measurements. The measurement  
396 setup consists of a diamond sample (S37, S52 or S79) with the Cx spectroscopic  
397 amplifier, a silicon diode with a C6 amplifier for a trigger and a  $^{90}\text{Sr}$  source on  
398 top. A particle emitted by the source traverses the sensor bulk and hits the silicon  
399 diode, triggering the analogue signal readout. The source is left on the top for the  
400 course of the experiment. The measurements, however, are taken at discrete times.  
401 For every data point, approximately  $10^4$  triggers are recorded. The offline analysis  
402 of the recorded signal pulse amplitudes yields a landau distribution for every data  
403 point. The most probable value (MPV) of the distribution is proportional to the  
404 collected charge by the diamond sensor. The resulting graph of charge collection over  
405 time (see figure 1.8) shows that the charge collection efficiency improves when the  
406 diamond sensor is primed with a  $\beta$  source. This is especially evident in the case of  
407 the two irradiated samples. S79 achieves close to a full efficiency whereas S52 reaches  
408 about 50 %. Both increases are significant. At a received dose of approximately  
409  $4 \times 10^6$  particles the signal stabilises. As expected, the signal of the non-irradiated

### 1.3. RADIATION LIMITATIONS

---

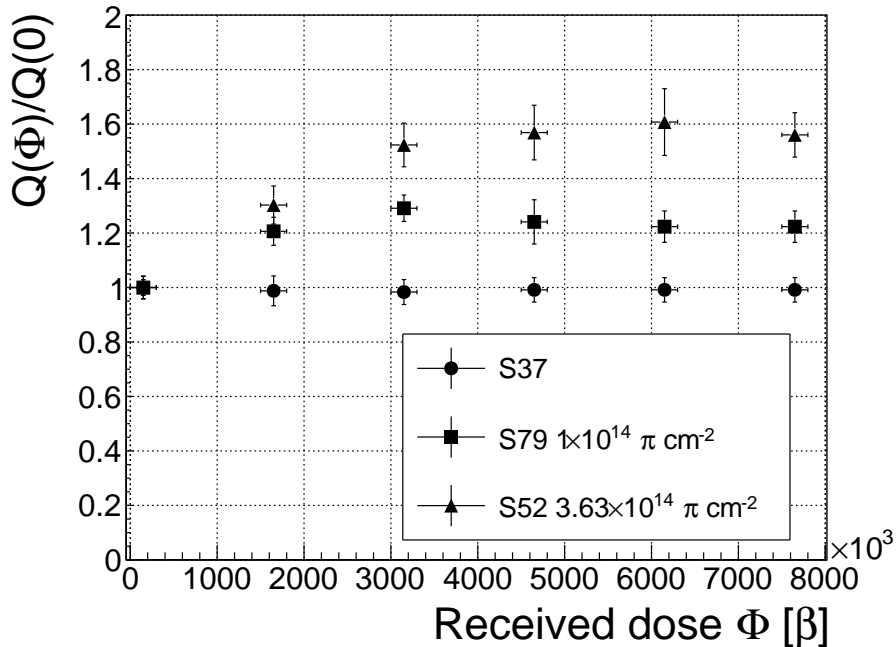


Figure 1.8: Relative increase of charge collection over time due to priming with the  ${}^{90}\text{Sr}$  radioactive source. The bias voltage for this measurement is 1 V/ $\mu\text{m}$ .

410 S37 does not change with time – this pure sCVD diamond sample has the maximum  
 411 collection distance from the start of the measurement.

412 It should be noted that the  $\sim 2.28$  MeV electrons emitted by this source are not  
 413 MIPs; their charge deposition is higher than that of an electron MIP, according to  
 414 the Bethe-Bloch distribution [7]. Nevertheless, for the purpose of these measurements  
 415 this energy was adequate since only the relative change in charge collection was of  
 416 our interest.

417 To sum up, diamond is a good choice for  $\beta$  radiation detection. Even if damaged  
 418 by radiation, it reaches a stable charge collection at a received dose of  $\sim 4 \times 10^6$  MIP  
 419 particles. The efficiency decreases with a high irradiation dose (effects visible above  
 420  $10^{12}$  MIP  $\text{cm}^{-2}$ ). However, the decrease can be accounted for if the damage factor  
 421 and the rate and energy of the particles are known.  $\gamma$  radiation has a similar impact  
 422 on the diamond as the  $\beta$  because the ionisation mechanism is the same. The incident  
 423 photons, if they interact with the diamond, prime the bulk, causing the increase in  
 424 charge collection efficiency. The difference, however, is that the interaction probability  
 425 (cross section) is lower for gammas [17, 10].

#### 426 $\alpha$ long-term stability

427 This part discusses the stability of irradiated diamond sensors during  $\alpha$  measurements.  
 428 An  ${}^{241}\text{Am}$  source is used, emitting  $\alpha$  particles with a mean energy of 5.5 MeV. It is  
 429 safe to assume that they will behave differently than when subject to  $\beta$  radiation.

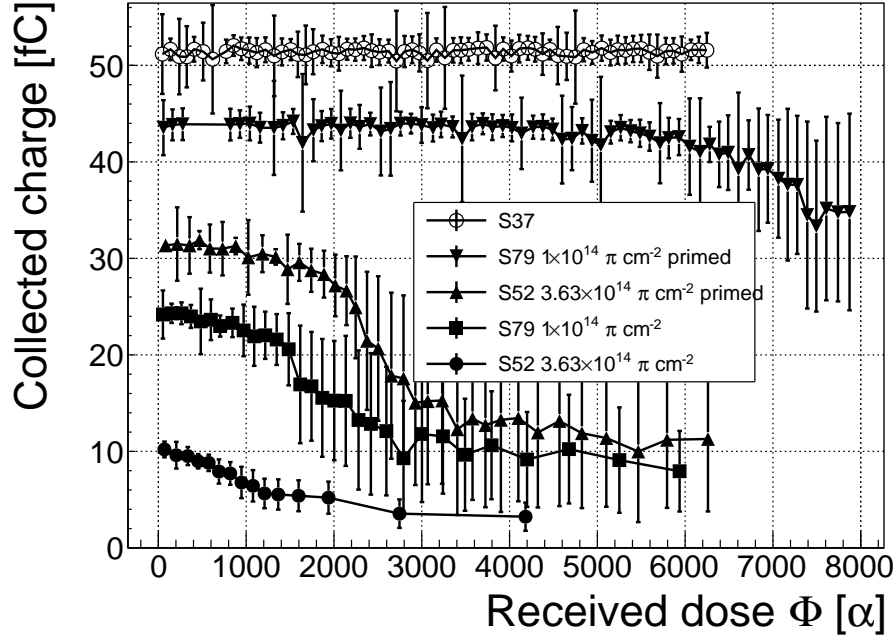


Figure 1.9: Comparison of collected charge with time for non-irradiated and irradiated diamond samples.

This is due to the point-like charge carrier creation when an  $\alpha$  particle penetrates the bulk and stops at a depth of  $\sim 14 \mu\text{m}$  (for a 5.5 MeV particle). The deposited energy produces  $\frac{5.5 \text{ MeV}}{13.6 \text{ eV}} = 4 \times 10^5 \text{ e-h pairs}$ . Compared to a MIP, which produces an MPV of  $500 \mu\text{m} \times 36 \text{ e-h } \mu\text{m}^{-1} = 18 \times 10^3 \text{ e-h pairs}$  in a  $500 \mu\text{m}$ , the collected charge is for a factor of 22 higher. In addition, the energy is deposited in a small volume –  $14 \mu\text{m}$  in depth and  $\sim 20 \text{ nm}$  radially [13]. This dense distribution of charge carriers affects their behaviour at the start of the drift. Furthermore, carriers of only one polarity drift through the sensor while those of the opposite polarity almost instantly recombine with the adjacent electrode. Taking into account that the diamond bulk has been damaged by irradiation, these two phenomena might have an effect on the operation of the detector on a macro scale.

The first test has been carried out using the Cx spectroscopic amplifier, with the bias voltage of the samples set to +500 V. Figure 1.9 shows the results of 6500 recorded hits at a rate of  $\sim 7$  particles per second. The collected charge for the non-irradiated sample is stable with time. It is expected that the irradiated samples will have a lower charge collection efficiency than the non-irradiated sample. However, their initial efficiency suddenly drops after a certain period of time. The initial efficiency is improved after priming with  $\beta$  particles, but eventually it deteriorates again. In addition, the spread of measured energies increases significantly. Finally, the particle counting rate decreases with the decreased efficiency.

To investigate this sudden drop in efficiency, the current pulse shapes using a C2 current amplifier have to be observed (see figure 1.10). The shape of the pulse

### 1.3. RADIATION LIMITATIONS

---

452 holds more information about the charge carrier properties in the sensor than solely  
453 the value of the integrated charge. This time only the primed S79 sample has been  
454 tested. Both hole and electron collection are observed to determine whether they  
455 behave differently or not. The sample has been measured long enough for the pulse  
456 shapes to start changing. The data in figures 1.10 show that the initially stable pulses  
457 start deteriorating – suddenly several different shapes start appearing, some still very  
458 similar to those from the beginning while the others with almost zero amplitude.

459 Some charges get stopped in the charge traps in the bulk for a long time, building  
460 up regions of space charge. The built up space charge affects the electric field, making  
461 it non-uniform. The non-uniform field in turn affects the drifting carriers, slowing  
462 them down or speeding them up, depending on the field gradient. Since the movement  
463 of the carriers is inducing the electric current, the field gradient can be observed in  
464 the signal.

465 The second test with the C2 current amplifier has been carried out as follows: At  
466 the beginning of the test when the diamond is still operating stably, 60 pulses are  
467 recorded. An average pulse is calculated. This is a reference pulse for the subsequent  
468 measurement points. Then an RMS of the single pulses with respect to the reference  
469 pulse is calculated and the values are summed together ( $\sigma_{\text{ref}}$ ).

470 All the subsequent data points also consist of a set of 60 pulses. At every data point  
471 the summation of the RMS values of the individual pulses with respect to the initial  
472 averaged pulse is calculated ( $\sigma$ ). The ratio between the initial  $\sigma_{\text{ref}}$  and discrete values  
473  $\sigma$  gives a measure of change of the pulse shape with respect to the reference pulse at  
474 the start of the measurement. Figure 1.11 shows the ratio  $\frac{\sigma_{\text{ref}}}{\sigma(\alpha \text{ dose})}$ . From the data  
475 obtained it can be concluded that initial pulse shape quickly starts deteriorating. In  
476 fact, the deterioration of the shape follows an approximate exponential decay function,  
477 which can be fitted to the data. The resulting decay constants for electrons and holes  
478 are  $\tau_e = (4400 \pm 150) \alpha^{-1}$  and  $\tau_h = (3300 \pm 140) \alpha^{-1}$ . The electrons retain the initial  
479 shape for longer. The deteriorated shapes also seem to be for a factor of 2 better  
480 than those of the holes.

481 Finally, an effort has made to find a way for the pulse shapes to return to their  
482 initial state. Five methods were tested:

- 483 1. Removing the source and leaving the bias voltage switched on,
- 484 2. Removing the source and switching the bias voltage off,
- 485 3. Priming with  $\gamma$  at a rate of  $400 \text{ s}^{-1}\text{cm}^{-1}$  without applied bias voltage,
- 486 4. Priming with  $\beta$  at a rate of  $1000 \text{ s}^{-1}\text{cm}^{-1}$  with applied bias voltage and
- 487 5. Priming with  $\beta$  at a rate of  $1000 \text{ s}^{-1}\text{cm}^{-1}$  without applied bias voltage.

488 The diamond sample S79 was first primed using a  $^{90}\text{Sr}$  source for about one hour.  
489 Then the bias voltage was switched on and an  $^{241}\text{Am}$  source was put on top. The  
490 pulses produced by the impinging  $\alpha$  particles had a proper rectangular pulse at the  
491 beginning, but then started changing in an erratic way, as described in the text above.

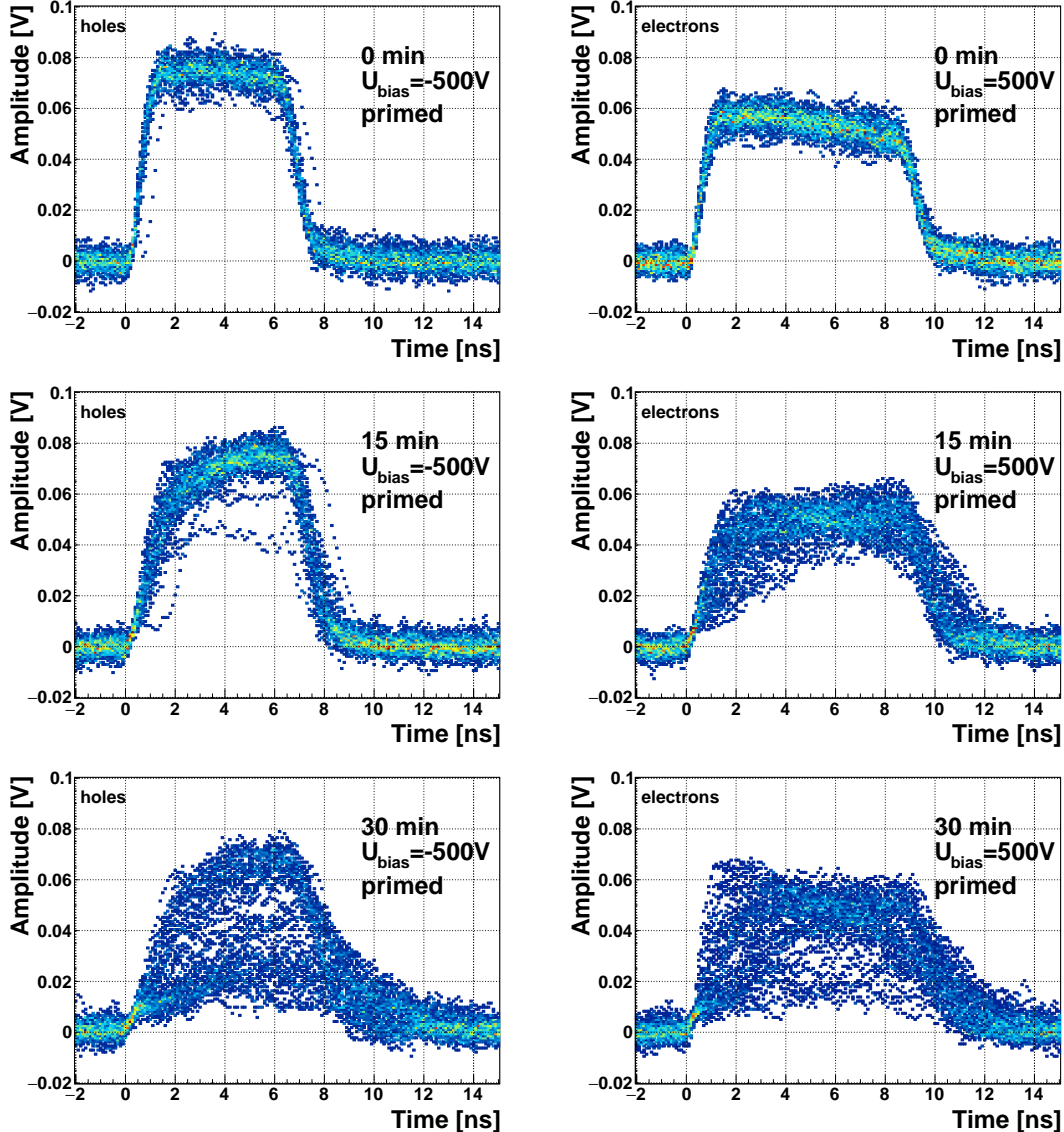


Figure 1.10: The signal of the irradiated and primed S79 deteriorates with time for both polarities. Every plot contains 60 superimposed pulses.

492 After approximately 30 minutes, one of the methods was tested. When a “healing”  
 493 procedure was started, a set of 60 pulses was taken at irregular points of time to  
 494 observe the change in the pulse shape and to assess the quality of the “healing”  
 495 procedure. Then the bias voltage was switched off and the sample was primed again  
 496 to reset its state before starting with the next run.

497 It turns out that the methods (3) and (5) improve the shape, method (2) helps  
 498 slowly, (1) does not show any change with time and (4) at first improves, but then  
 499 significantly degrades the shape. The effect observed in method (4) has already been  
 500 described in [14]. The “healing” process therefore depends on the rate of radiation,  
 501 the bias voltage and the time of exposure. The ionising radiation creates free charges,

### 1.3. RADIATION LIMITATIONS

---

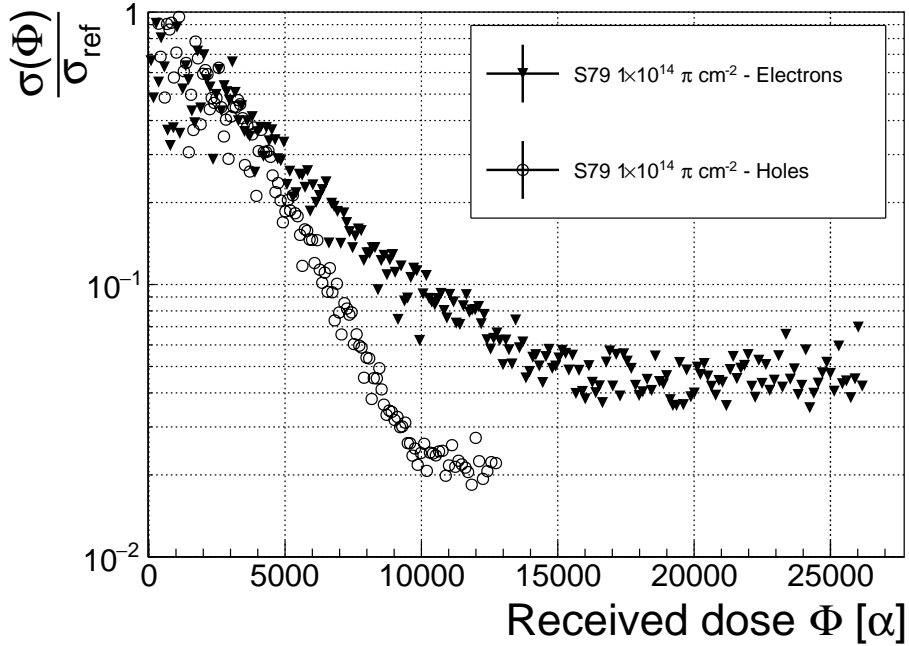


Figure 1.11: Deterioration of the pulse shapes with time

502 which quickly recombine close to the place of generation. It is likely that they also  
 503 release the charges trapped during the measurement, reducing the overall effect of  
 504 the space charge. The traps get filled with both flavours of carriers, thus they are  
 505 neutralised. The pulse shape gradually returns to its initial state.

Procedure	Source	Bias voltage	Effectiveness
1	/	ON	no
2	/	/	slow
3	$^{60}\text{Co}$	/	YES
4	$^{90}\text{Sr}$	ON	no
5	$^{90}\text{Sr}$	/	YES

507 Table 1.2: Effectiveness of healing procedures

508 In summary, the shape of the pulses caused by  $\alpha$  radiation changes with time  
 509 for irradiated samples. The shape of the pulses gets distorted and becomes erratic.  
 510 Charge collection decreases and its spread increases. This happens even faster for  
 511 non-primed diamonds. To “heal” the diamond – to bring the pulse shapes back to  
 512 their initial shape – the sample must be primed using a  $\beta$  or a  $\gamma$  source for several  
 513 minutes at the bias voltage set to 0 V. Switching to the inverse polarity for a few  
 514 seconds helps a bit, but in a long run distorts the signal, which cannot get back to  
 515 its initial shape.

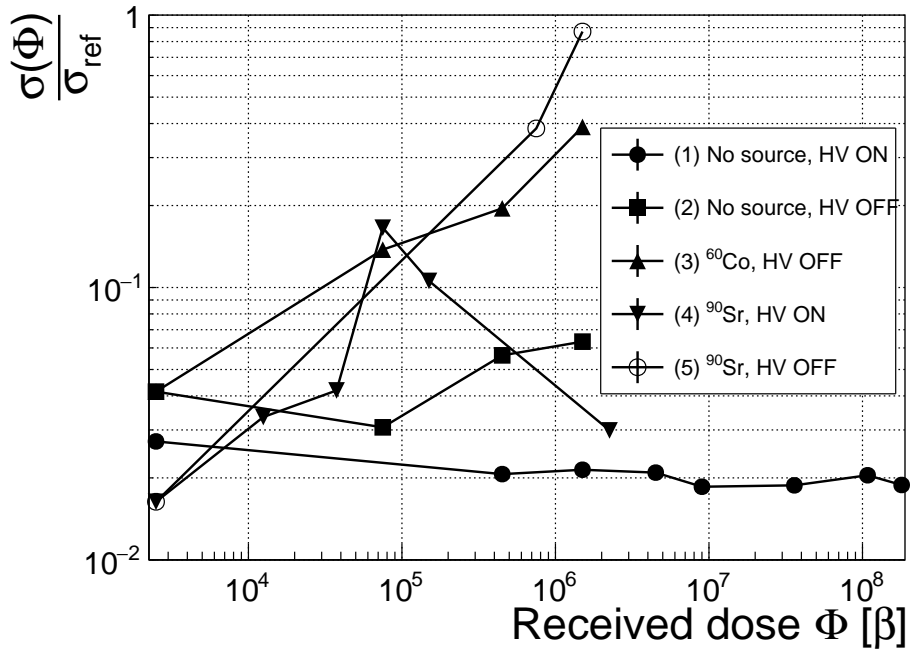


Figure 1.12: Five procedures for the “healing” process for an irradiated diamond that was exposed to  $\alpha$  radiation at bias voltage switched on for at least 30 minutes at a rate of  $10^4 \text{ s}^{-1}$ .

## 516 1.4 Temperature limitations

517 A test has been carried out to evaluate the effect of temperature changes on the  
 518 output signal of the diamond sensors. A cryostat filled with liquid helium is used to  
 519 cool down the sensor during the measurement process. The current signal response  
 520 to  $\alpha$ -particles is measured at 18 temperature points between 4 K and 295 K. At every  
 521 temperature point, a set of 300 pulses is read out at various bias voltages. Resulting  
 522 data show that the charge collection is stable down to 150 K, where it starts decreasing  
 523 and stabilises again at about one third of the initial value at 75 K. This behaviour  
 524 was first measured and discussed by H. Jansen [13].

525 The band gap energy in diamond is equal to  $E_g = 5.5 \text{ eV}$  while the average  
 526 energy to produce an electron-hole pair is  $E_{e-h} = 13.25 \text{ eV}$ . This means there is  
 527 excessive energy deposited in the diamond bulk. The incident  $\alpha$ -particle stops within  
 528  $\sim 10 \mu\text{m}$  of the bulk, transferring all its energy to the lattice. A part of this energy,  
 529 approximately 40 % [13], directly ionises the carbon atoms, creating free electron-hole  
 530 pairs. The positively charged hole and the negatively charged electron in the hole  
 531 attract each other via the Coulomb force and may undergo a bonding process during  
 532 which a phonon is emitted.

533 The remaining energy, however, is converted into lattice vibrations (phonons [18]).  
 534 This means that the lattice within the ionisation volume (approximately  $\sim 15 \mu\text{m} \times \sim 2 \text{ nm}$   
 535 in size) is briefly heated up. The hot plasma then cools down to the temperature of

## 1.4. TEMPERATURE LIMITATIONS

---

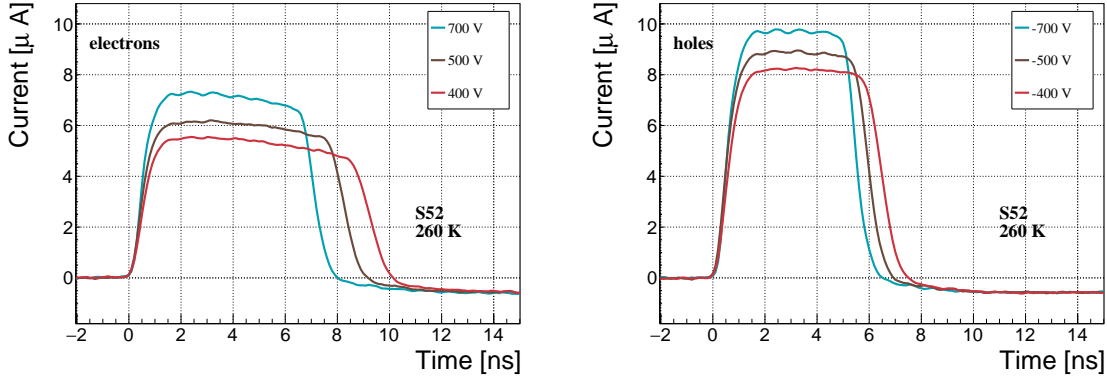


Figure 1.13: Varied bias voltage at a fixed temperature

the surrounding material by heat dissipation, (i.e. phonon transport). The free electron binds the free hole into a bound state (not recombination) – the exciton [15]. The exciton binding energy is 80 meV. At higher temperatures, the lattice provides enough energy to excite the electron from the exciton state back to the conduction band. At lower temperatures, however, the exciton lifetime increases, which means that it will take a longer time for the electrons to get re-excited to the conduction band. The re-excitation lifetime at room temperature is  $\sim 30$  ps, increasing to  $\sim 150$   $\mu$ s at 50 K [13]. This means that some of the bound electrons will not even start drifting within the period of  $\sim 10$  ns, which is the expected carrier drift time. When they are finally freed, the current they induce is already hidden in the electronics noise. The effective area of the observed current pulse is therefore smaller than that of a pulse induced by all the carriers drifting at the same time. This in effect reduces the measured collected charge. The longer the time constant, the lower the measured collected charge, as shown in figure 1.17 below.

### 1.4.1 Temperature-variant $\alpha$ -TCT before irradiation

Three sCVD diamond samples have been tested at a range of temperatures using the  $\alpha$ -TCT technique. At each temperature point, the bias voltage is set to several positive and negative values. A set of 300 pulses is recorded at every data point and averaged offline. The resulting averaged pulses of sample S37 at the 260 K temperature point and a bias voltage of  $\pm 400$  V,  $\pm 500$  V and  $\pm 700$  V are shown in figure 1.13. The pulses induced by holes as charge carriers are shorter than those induced by electrons, which means that holes travel faster in diamond. The area of the pulse, however, is the same for both polarities, which corresponds to the fact that the same amount of charges is drifting in both cases.

Figure 1.14 shows pulses at a bias voltage set to  $\pm 500$  V across the range of temperatures between 4 K and 295 K – room temperature (RT). Several conclusions can be drawn by observing their shape. First, the pulse shapes change with decreasing temperature. The pulse time gets shorter, hinting at the faster carrier drift velocity

564  $v_{\text{drift}}$ . Second, between 150 K and 75 K there is a significant change in shape - the  
565 time constant of the rising edge increases significantly and the pulse area decreases.  
566 From 75 K down to 4 K there is no significant observable change. Last, the top of  
567 the pulse at the S52 is not flat, which means that a portion of the drifting charge is  
568 lost along its way. This is due to charge trapping, likely by means of crystal defects  
569 or impurities.

#### 570 1.4.2 Temperature-variant $\alpha$ -TCT after irradiation

571 The irradiated S79 and S52 have been re-tested in the cryostat after irradiation.  
572 The aim was to see how their pulse shapes change with decreasing temperature,  
573 in particular the decaying top of the pulses (see figure 1.15). The decay time gives  
574 information on trapping of charge carriers while travelling through the diamond bulk.  
575 A variation of the decay time constant as a function of temperature might help to  
576 reveal the type and depth of the charge traps. To observe these effects or lack thereof,  
577 a number of requirements has to be met. First, the diamond samples are intentionally  
578 not primed prior to the experiment because priming would improve the pulse shapes  
579 and possibly change the decay time constant of the signal. Second, keeping in mind  
580 that the pulse shape of irradiated diamonds changes with time, the duration of the  
581 measurement of an individual data point has to be short – of the order of 30 seconds.  
582 Last, the sequence of the bias voltage settings is important, the reason for which is  
583 explained below.

584 Unfortunately it is not possible to avoid temporal pulse changes. For instance,  
585 one measurement point takes approximately one minute. After the measurement, the  
586 bias voltage polarity is swapped for a few seconds to bring the diamond back into its  
587 initial state. But a few seconds with respect to a minute is not enough. Therefore,  
588 when the bias voltage is set to the next value, there is still some residual effect of  
589 the previous measurement. Similar to the effects of polarisation, this effect is also  
590 decreasing the pulse height. This can be observed in figure 1.15, which shows the  
591 resulting pulses of S52 for bias voltages of  $\pm 200$  V,  $\pm 300$  V,  $\pm 400$  V and  $\pm 500$  V  
592 at 230 K and 260 K. In this case the measurements sequence is: 230K (200 V,  
593 300 V, 400 V, 500 V, -500 V, -400 V, -300 V), 260 K (-200 V, -300 V, -400 V, -  
594 500 V, 500 V, 400 V, 300 V). The changes in pulse shapes for holes at 230 K and  
595 260 K cannot be attributed to the temperature change. Instead, the explanation  
596 could lie in diamond “polarisation”. This means that, when exposed to an electric  
597 field with  $\alpha$  measurements ongoing, the diamond builds up an internal electric field  
598 of inverse polarity, which effectively reduces the overall electric field. This internal  
599 field does not dissipate when the external bias voltage is switched off. It can be  
600 said that the diamond becomes “polarised”. When switching the polarity of the  
601 external bias voltage, the internal and external electric field point in the same direction  
602 at the beginning, increasing the overall electric field and with it the pulse height.  
603 In figure 1.15, this happens when switching from 500 V (figure 1.15a) to -500 V  
604 (figure ??) at 230 K. The built up polarisation contributes to the pulse having a

#### 1.4. TEMPERATURE LIMITATIONS

---

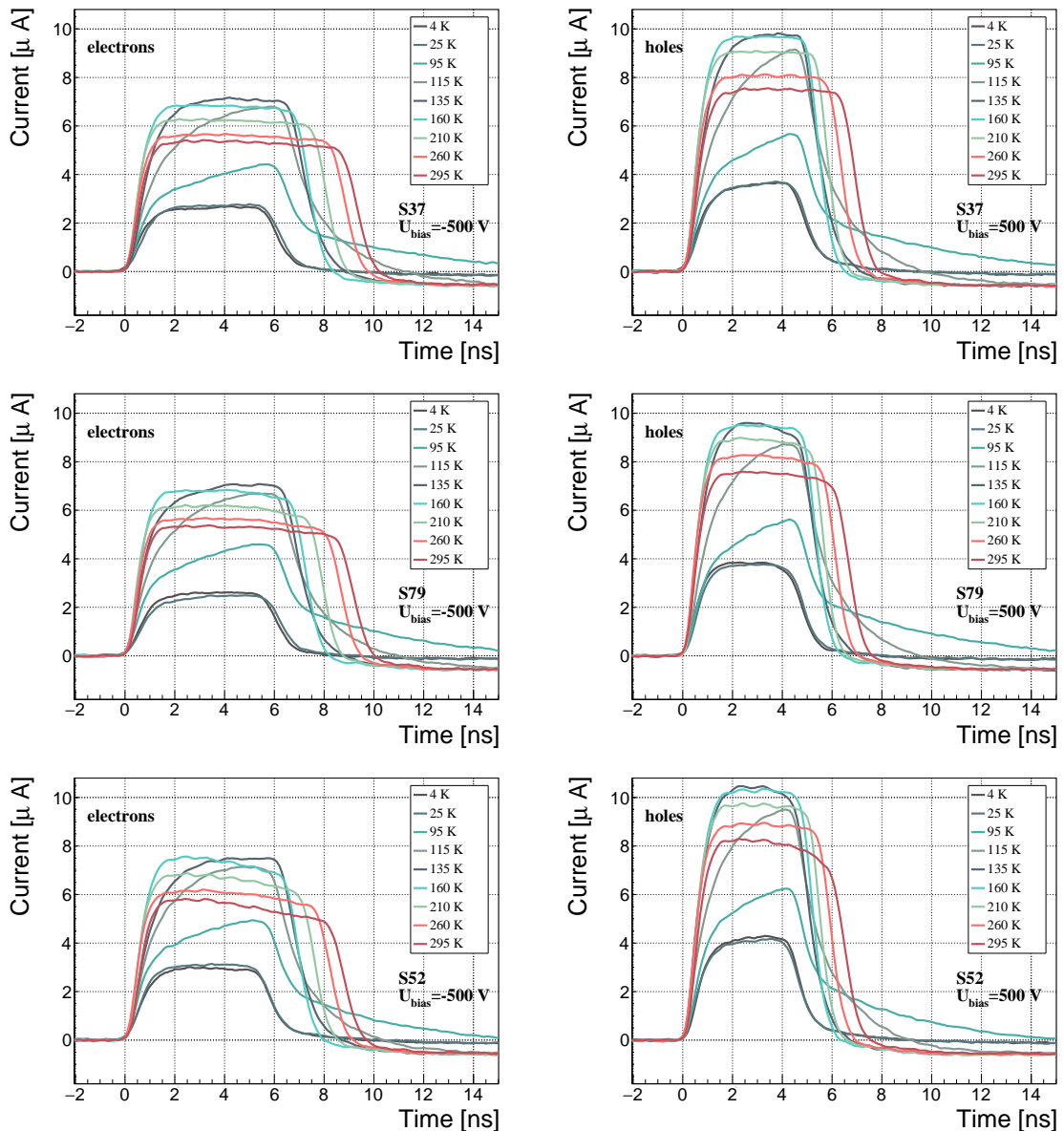


Figure 1.14: Several data points between 4 K and 295 K at a bias voltage of  $\pm 500$  V

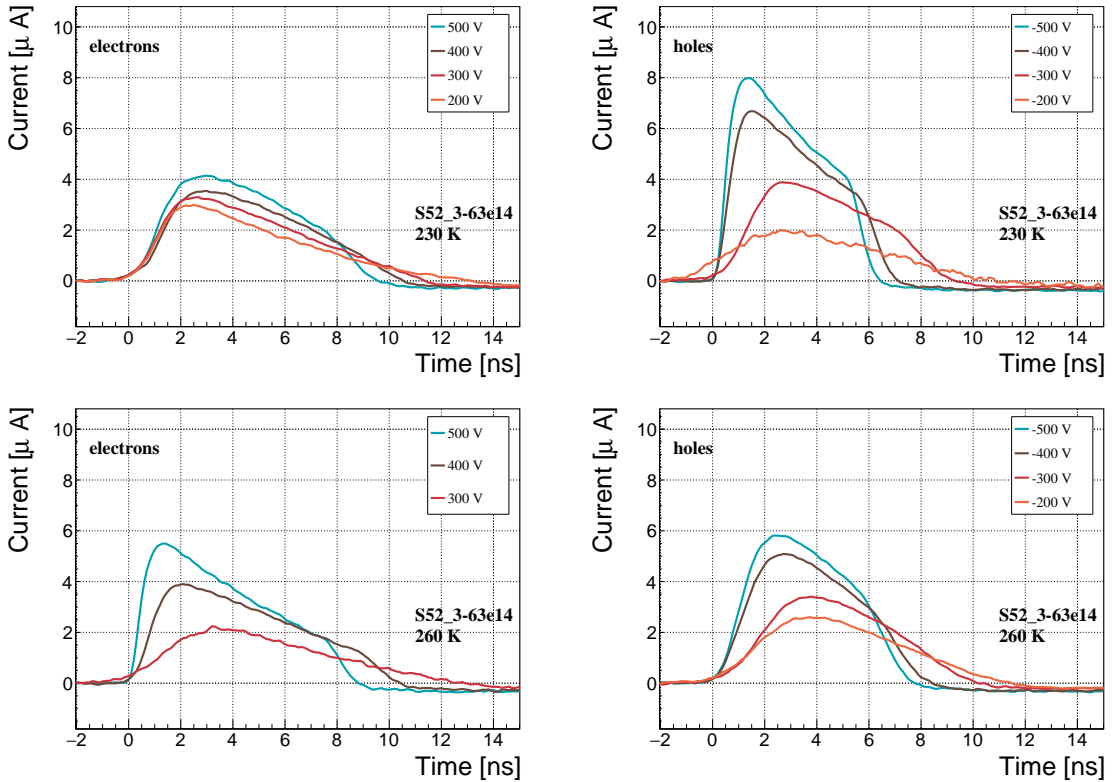


Figure 1.15: Varied bias voltage at a fixed temperature for an irradiated sample

sharp rising edge and a high amplitude. This effect decays during the next two voltage points. There would be a handful of ways to avoid this polarisation effect in the data:

1. After every data point invert the bias voltage and leave it to return to a neutral state for the same amount of time,
2. Make a hysteresis of data points, going from minimum negative to maximum positive bias several times,
3. Reduce the measurement time at every bias voltage setting.

Unfortunately, options (1) and (2) are very time consuming and would increase the overall experiment time to over one day. The third option would worsen the resulting averaged pulses. In the end an alternative option was chosen: alternating the starting bias voltage and the sequence at every temperature point. With this option, a meaningful systematic error in analysing the pulse shapes can be attained.

Figure 1.16 shows the irradiated S52 and S79 as well as the non-irradiated S37 for comparison, all at a bias voltage of  $\pm 500$  V and at several temperature points between 4 K and RT. It is evident that the radiation damage affected the shape of the pulses across all temperatures.

## 1.4. TEMPERATURE LIMITATIONS

---

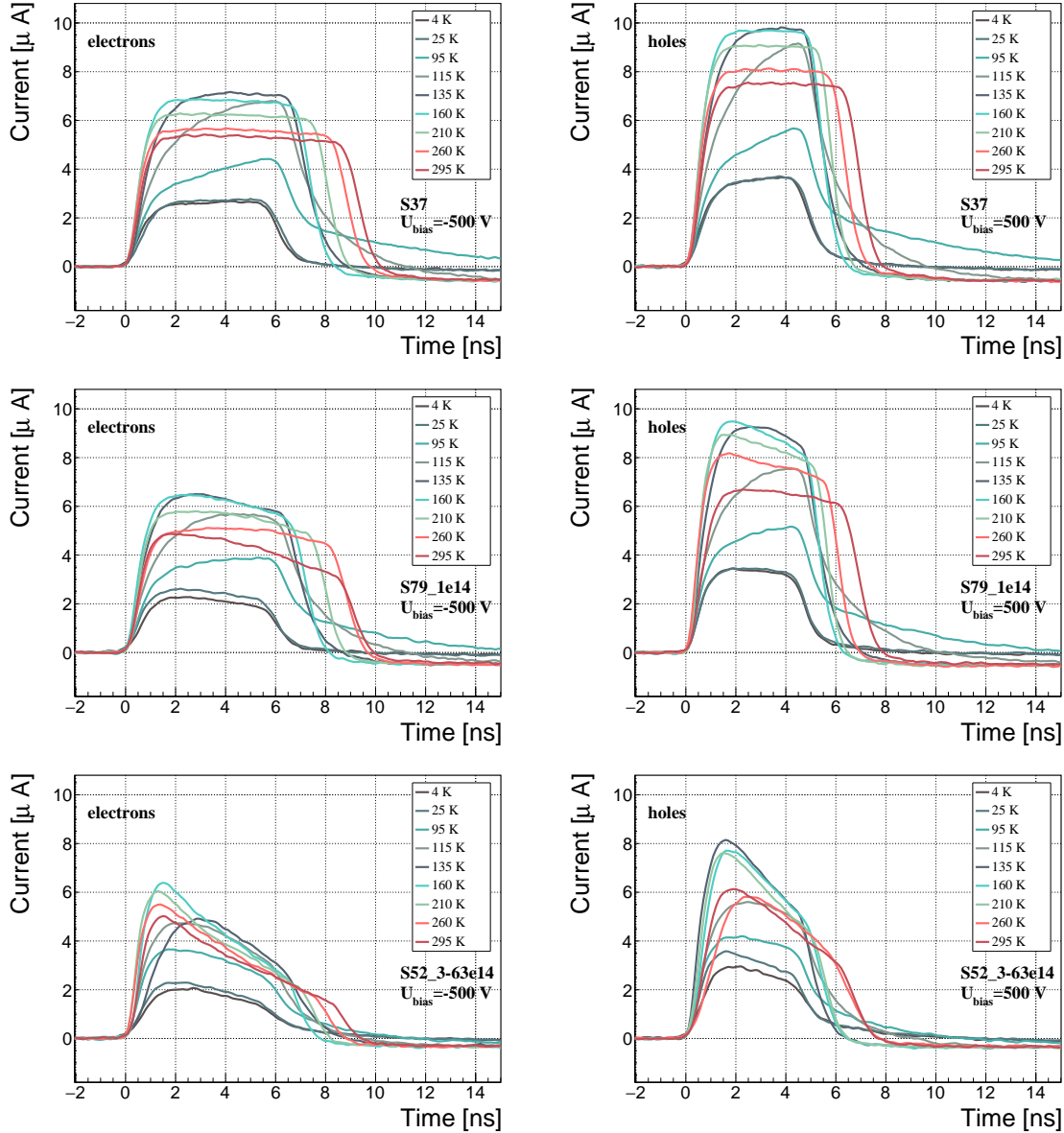


Figure 1.16: After irradiation: several data points between 4 K and 295 K at a bias voltage of  $\pm 500 \text{ V}$

### 622 Collected charge as a function of temperature

623 The area below the current pulse is proportional to the charge collected by the dia-  
 624 mond detector. The collected charge is observed as a function of temperature. First,  
 625 the amplitude values of the averaged pulses at a bias voltage of  $\pm 500 \text{ V}$  and across the  
 626 temperature range between 4 K and 295 K have to be integrated. Then a calibration  
 627 factor is used to derive the charge for all data points. This factor is obtained using  
 628 a Cx charge-sensitive amplifier. The resulting values for electrons and holes are plot-  
 629 ted in figures 1.17a and 1.17b, respectively. Thesis [13] gives a model that explains

the drop in charge below 150 K. The new contribution are the data points for the irradiated samples. The values for them are lower than the those of non-irradiated samples, which is expected.

The values for all samples are fairly stable in the range between 4 K and 75 K and between 150 K and 295 K. However, in the values for the irradiated S52 some excursions can be observed. This is due to the sequence of the measurement steps, which introduced a hysteresis effect and is explained in the preceding text.

The collected charge drops significantly from 150 K down to 75 K. In the non-irradiated samples the values in the lower temperature range are approximately 0.30 of the values at the high range. For the irradiated ones this difference is lower – a factor of 0.35 for S79 and 0.5 for S52. An interesting detail is that the ratio between the values for non-irradiated samples and their irradiated counterparts at the lower range is different than at the higher range. Looking at the values for the electron collection in figure 1.17a: for S52 the lower ratio is equal to 1.28 and the higher equal to 1.7. For S79 these ratios are 1.00 and 1.09, which means that the difference in charge collection between 4 K and 75 K before and after irradiation is negligible.

#### Charge trapping

The carriers drifting through the bulk get stopped by the charge traps with a certain probability. This trapping happens uniformly throughout the diamond, decreasing the number of carriers in the charge cloud. Therefore the absolute number of trapped carriers decreases. At the same time the absolute number of trapped carriers per unit of length decreases. The resulting function for the number of drifting carriers per unit of length is a decaying exponential function:

$$I(t) = I(0) \cdot e^{-\frac{t-t_0}{\tau}} + I_0, \quad (1.6)$$

where  $I(0)$  is the initial induced current,  $I_0$  is the end current,  $t$  is time,  $t_0$  is temporal displacement of the pulse and  $\tau$  is the decay time constant. This value tells how long it takes before the amplitude of the pulse decreases to 63 % of its initial height.

The decaying exponential function has been fitted to the decaying top of the averaged pulses at bias voltages of  $\pm 400$  V and  $\pm 500$  V across all temperatures excluding the transitional range between 75 K and 150 K. The resulting decay time constants  $\tau$  for an individual temperature point are not equal, which stems from the fact that the pulses change with time due to “polarisation”. This counts as a systematic error. Therefore the fitted  $\tau$  for  $\pm 400$  V and  $\pm 500$  V are averaged into one value representing the measurement at that temperature point. Figure 1.18a shows the fitted  $\tau$  for the five samples between 4 K and 295 K. In principle, the time constants should be infinite for a perfect and non-irradiated sample. Here a slightly tilted top of the pulse due to space charge is already successfully fitted with an exponential function, resulting in a  $\tau$  of the order of  $(200 \pm 20)$  ns<sup>-1</sup>. Consequently the fitting method is not adequate for non-irradiated samples. For the irradiated samples, the fit becomes increasingly more meaningful. As seen in figure 1.18a, the

#### 1.4. TEMPERATURE LIMITATIONS

---

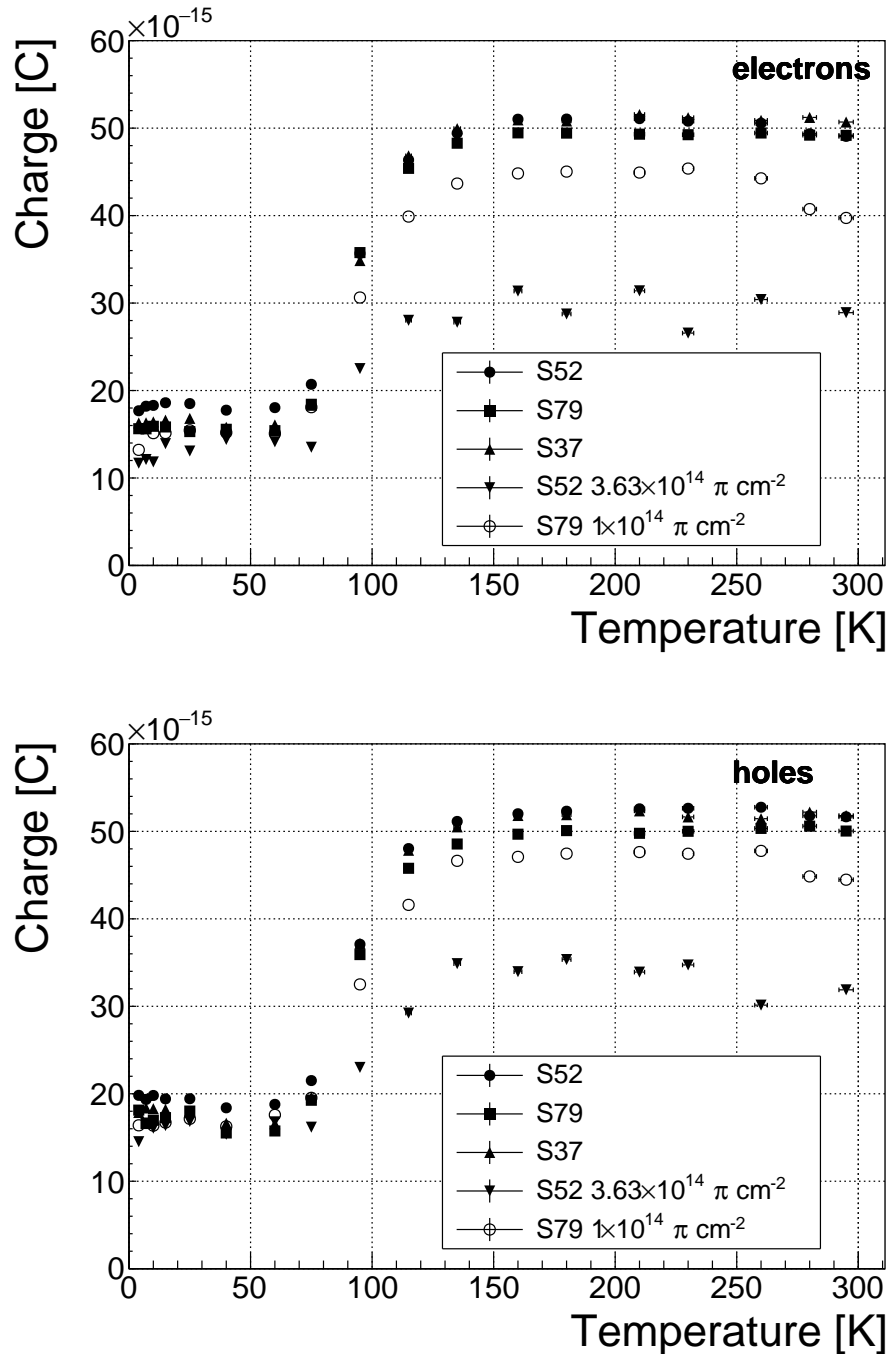


Figure 1.17: Collected charge as a function of temperature

fitted values of the irradiated samples are fairly stable across all temperatures. There  
 is a slight increase in the decay time constant of the S52 from  $(6.0 \pm 0.5) \text{ ns}^{-1}$  above  
 150 K to  $(8.5 \pm 0.9) \text{ ns}^{-1}$  below 75 K. On the other hand, this step is not observable  
 in the S79 data. With only one sample exhibiting this behaviour, the effect is not  
 significant enough. Judging by the data acquired, the samples would need to be

*CHAPTER 1. EXPERIMENTAL RESULTS*  
*DIAMOND IRRADIATION STUDY*

---

674 irradiated to doses above  $1 \times 10^{14} \pi \text{ cm}^{-2}$  to quantify this effect in detail. So far  
675 this effect will not be regarded as significant for the scope of this thesis. Building on  
676 this assumption, the conclusion is that the signal decay time constant for irradiated  
677 sCVD diamond is constant across the temperature range between 4 K and 195 K,  
678 excluding the transitional range between 75 K and 150 K.

679 Taking into account the conclusions above, all the values can be averaged into one  
680 decay constant. Figure 1.18b shows these values for all samples as a function of the  
681 received  $\pi_{300 \text{ MeV}}$  radiation dose. To estimate the carrier lifetime with respect to the  
682 radiation dose received, a similar model is used than that in section 1.5. This model  
683 states that the inverse of the carrier lifetime is linearly decreasing with increasing  
684 radiation dose:

$$\frac{1}{\tau} = \frac{1}{\tau_0} + \kappa_\tau \cdot \Phi \quad (1.7)$$

685

$$\tau = \frac{\tau_0}{\kappa_\tau \tau_0 \Phi + 1} \quad (1.8)$$

686 where  $\tau_0$  is the lifetime for a non-irradiated sample (real lifetime, therefore of the order  
687 of  $400 \text{ ns}^{-1}$ ),  $\tau$  is the lifetime of an irradiated sample,  $\Phi$  is the received radiation dose  
688 and  $\kappa_\tau$  the lifetime degradation factor. For these data the fitted factor is equal to  
689  $\kappa_\tau = (3.6 \pm 0.8) \times 10^{-16} \text{ s cm}^2 \pi_{300 \text{ MeV}}^{-1}$ . Using this factor, the steepness of the decay  
690 in the pulse shape with respect to radiation dose can be estimated. This can help  
691 when designing a system where current pulse shape is an important factor.

#### 1.4. TEMPERATURE LIMITATIONS

---

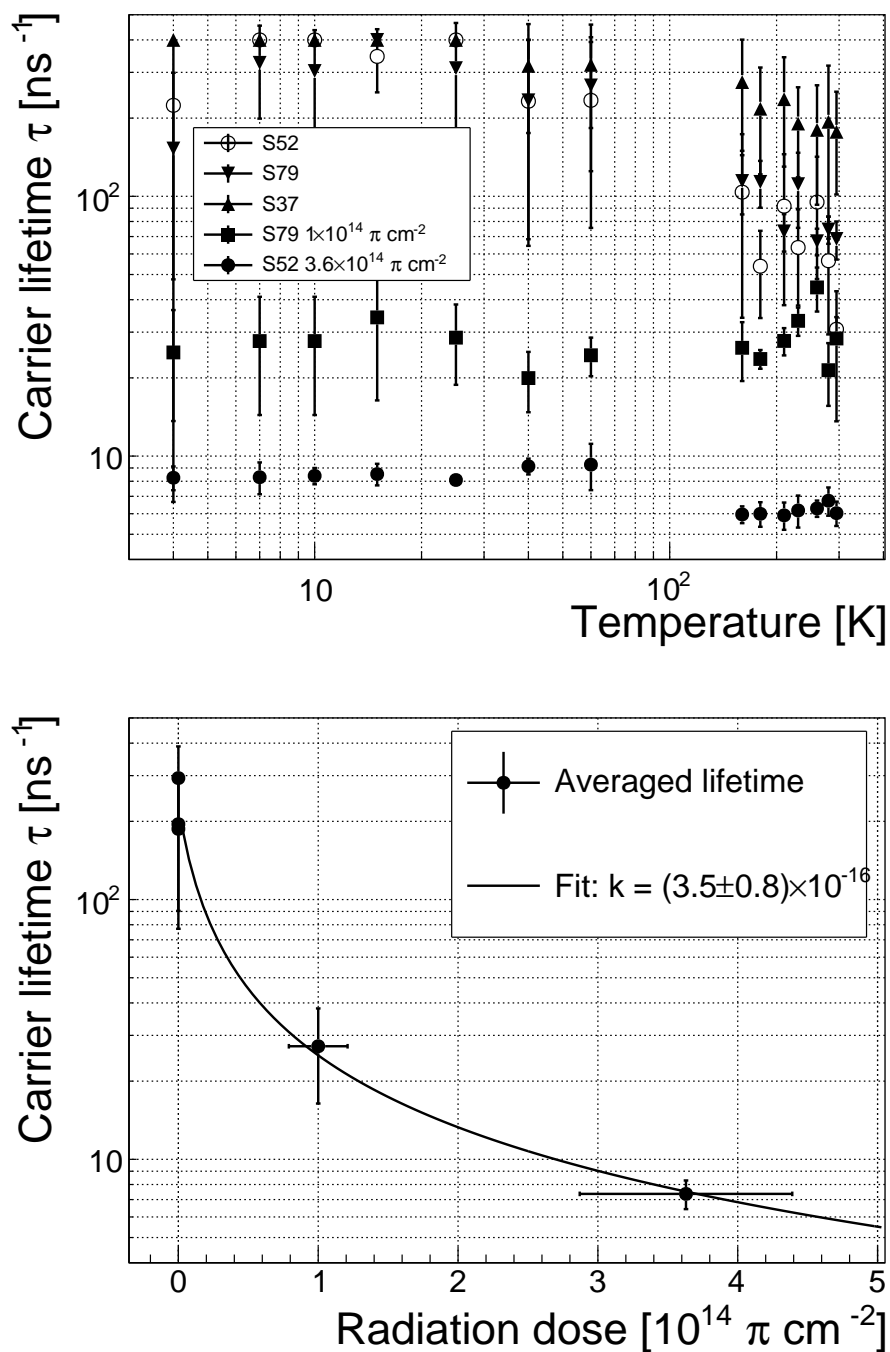


Figure 1.18: Charge carrier lifetime decreases with irradiation, but is stable across the range of temperatures between 4 K – 75 K and 150 K – 295 K. The first figure shows the carrier lifetime  $\tau$  as a function of temperature whereas the second figure depicts the carrier lifetime averaged over all temperatures and plotted against the  $\pi$  irradiation dose

692 **1.5 Conclusion**

693 This chapter gives an overview of the capabilities and limitations of diamond as  
694 a particle detector. Three effects on diamond were studied – noise, radiation and  
695 temperature, the focus being on the latter two.

696 Two sCVD diamond detectors were irradiated with 300 MeV pions. They were  
697 tested alongside a non-irradiated sample to observe the changes in the ability to detect  
698  $\alpha$ ,  $\beta$  and  $\gamma$  radiation. Their charge collection efficiency was measured in a test beam  
699 facility using . The results were compared to the results from the RD42 collaboration  
700 and a DPA model. A radiation damage factor  $k_\lambda = (3.0 \pm 1.0) \times 10^{-18} \mu\text{m}^{-1} \text{cm}^{-2}$  was  
701 obtained for  $\pi_{300 \text{ MeV}}$  particles. The data point was not in agreement with the data  
702 provided by RD42 nor with the model. However, the irradiation process and the low  
703 number of tested samples hold a relatively high statistical uncertainty. In addition,  
704 there was no diamond surface treatment done in between the measurements, as is the  
705 case in the study conducted by RD42. The results obtained in the course of these  
706 measurements will also be fed into the existing pool of data in the RD42 collaboration.

707 The next step was to test the long-term capabilities for  $\alpha$  detection. The shape  
708 of the ionisation profile was investigated to determine the behaviour of the charge  
709 carriers in the irradiated diamond. An exponential decay was observed in the pulses  
710 of irradiated samples, proving that there are charge traps in the bulk that were created  
711 during irradiation. Then a long-term stability test was carried out. The results show  
712 that the irradiated diamond detectors do not provide a stable and reliable long-term  
713 measurement of  $\alpha$  particles. This might be due to a space-charge build-up in the  
714 bulk, which changes the electric field, affecting the charge carriers. A procedure to  
715 improve the pulse shape using  $\beta$  and  $\gamma$  radiation was proposed.

716 Finally, the diamond sensors were cooled down to temperatures between 4 K and  
717 295 K. Their response to  $\alpha$  particles was observed. The results of the non-irradiated  
718 and irradiated samples were compared. The effect of reduction for the number of  
719 drifting charges due to exciton recombination was observed in both sets of data.  
720 The second set had a superimposed effect of charge trapping during the drift, which  
721 was represented by an exponential decay in the signal. The decay time constant  
722 did not change with temperature. Therefore all temperature points for individual  
723 samples were averaged and the decay time constants were plotted against the received  
724 radiation dose. A damage factor equal to  $\kappa_\tau = (3.5 \pm 0.8) \times 10^{-16} \text{ s cm}^2 \pi_{300 \text{ MeV}}^{-1}$  for  
725 non-primed diamonds was defined.

## <sup>726</sup> Bibliography

- <sup>727</sup> [1] *DRS4*. <https://www.psi.ch/drs/evaluation-board>.
- <sup>728</sup> [2] *Element Six*. <http://www.e6.com>.
- <sup>729</sup> [3] *IHa Technologies Pte. Ltd.* <https://www.2atechnologies.com>.
- <sup>730</sup> [4] *Paul Scherrer Institute*. <https://www.psi.ch/>.
- <sup>731</sup> [5] *RD42 collaboration*. <http://rd42.web.cern.ch/rd42/>.
- <sup>732</sup> [6] *Determination of operational dose equivalent quantities for neutrons*. ICRU,  
<sup>733</sup> Washington, DC, 2001.
- <sup>734</sup> [7] H. Bethe and J. Ashkin. *Experimental Nuclear Physics*, ed. E. Segre, page 253,  
<sup>735</sup> 1953.
- <sup>736</sup> [8] Giorgio Brianti. SPS North Experimental Area. Technical Report CERN-SPSC-  
<sup>737</sup> T-73-8. LabII-EA-Note-73-4, CERN, Geneva, 1973.
- <sup>738</sup> [9] P. Carazzetti and H. R. Shea. *Electrical breakdown at low pressure for planar  
739 microelectromechanical systems with 10- to 500  $\mu\text{m}$  gaps*. *J. Micro/Nanolith.  
740 MEMS MOEMS*, (8(3), 031305), Jul-Sep 2009.
- <sup>741</sup> [10] E. Griesmayer and B. Dehning. Diamonds for beam instrumentation. *Physics  
742 Procedia*, 37:1997 – 2004, 2012. Proceedings of the 2nd International Conference  
743 on Technology and Instrumentation in Particle Physics (TIPP 2011).
- <sup>744</sup> [11] Moritz Guthoff, Wim de Boer, and Steffen Mller. Simulation of beam induced  
745 lattice defects of diamond detectors using {FLUKA}. *Nuclear Instruments and  
746 Methods in Physics Research Section A: Accelerators, Spectrometers, Detectors  
747 and Associated Equipment*, 735:223 – 228, 2014.
- <sup>748</sup> [12] M. Huhtinen. Simulation of non-ionising energy loss and defect formation in  
749 silicon. *Nuclear Instruments and Methods in Physics Research A*, 491:194–215,  
750 September 2002.
- <sup>751</sup> [13] Hendrik Jansen, Norbert Wermes, and Heinz Pernegger. *Chemical Vapour De-  
752 position Diamond - Charge Carrier Movement at Low Temperatures and Use in*

## BIBLIOGRAPHY

---

- 753        *Time-Critical Applications*. PhD thesis, Bonn U., Sep 2013. Presented 10 Dec  
754        2013.
- 755        [14] Gregor Kramberger, V. Cindro, A. Gorisek, I. Mandic, M. Mikuz, and M. Zavr-  
756        tanik. Effects of bias voltage during priming on operation of diamond detectors.  
757        *PoS*, Vertex2012:013, 2013.
- 758        [15] W. Y. Liang. Excitons. *Physics Education*, 5:226–228, July 1970.
- 759        [16] M. Mikuž. *Diamond sensors for high energy radiation and particle detection*.  
760        [https://indico.cern.ch/event/102998/session/22/contribution/463/attachments/10561/15445/  
761        TIPP11-nb.pdf](https://indico.cern.ch/event/102998/session/22/contribution/463/attachments/10561/15445/TIPP11-nb.pdf), TIPP, 2011.
- 762        [17] V. Sarin. *Comprehensive Hard Materials*. Elsevier Science, 2014. p. 411.
- 763        [18] J. L. Yarnell, J. L. Warren, and R. G. Wenzel. Lattice vibrations in diamond.  
764        *Phys. Rev. Lett.*, 13:13–15, Jul 1964.